arXiv:1512.06119v2 [cond-mat.mtrl-sci] 8 Jun 2016

Swift Heavy Ion Irradiation-Induced Modifications in Structural, Optical, Electrical and Magnetic Properties of Mn Doped $SnO_{2-\delta}$ Thin Films

Sushant Gupta[1*], Fouran Singh[2], B. Das[1]

[1] Department of Physics, Lucknow University, Lucknow-226007, India
[2] Inter University Accelerator Centre (IUAC), New Delhi-110067, India
*E-mail: sushant1586@gmail.com

Abstract

Swift heavy ion irradiation is an effective technique to induce changes in the lattice of the materials leading to significant modification of properties. In this paper, we have presented the impact of swift heavy ion beam irradiation on the structural, optical, electrical and magnetic properties of $Sn_{0.9}Mn_{0.1}O_{2-\delta}$ thin films. Measurement of resistivity, mobility, carrier density, transmissivity to visible light, and saturation magnetization as a function of ion fluence (1×10^{11} to 3×10^{13} $ions/cm^2$) promulgates that increasing fluence results in degradation in electrical, optical and magnetic properties of $Sn_{0.9}Mn_{0.1}O_{2-\delta}$. The structural, optical and electrical results have been interpreted by using properties of native or point defects, whereas the magnetic and morphological variations have been explained in terms of conductivity of material. Efforts have been made to summarize the properties of all possible charged and neutral point defects (V_{Sn}^{4-}, Sn_i^{4+}, V_O^0, O_i^{2-}, Sn_O^{4+}, O_{Sn}^{2-}, H_O^+) and afterwards from the correlation between experimentally-observed and theoretically-calculated results various interesting conclusions have been drawn.

Keywords:- Swift heavy ion; Transparent conducting oxide; Dilute magnetic semiconductor; Thin films; Point defects.

1. Introduction

Transparent conducting oxides (TCO) are a unique class of material that combines two features, electrical conductivity and optical transparency, which are not typically found in the same material [1-4]. A good TCO material should have a carrier concentration of the order of 10^{20} cm^{-3}, a resistivity of the order of 10^{-3} Ω cm, and an optical transmission above 80% in the visible range of the electromagnetic spectra. Tin oxide (SnO_2) thin films with such unique features have been extensively used in optoelectronic applications for flat panel displays, smart windows, solar cells, and electromagnetic interference shielding windows [5, 6]. Recently there is an increased interest to introduce magnetic functionality in tin oxide semiconductors due to their promising applications in spintronics [7-12]. The tin oxide semiconductor can be made ferromagnetic by doping with transition-metal (TM) ions. The first report of high Curie temperature ferromagnetism in tin oxide thin films was by Ogale et. al. [13], who reported a Curie temperature T_c = 650 K in pulsed laser deposited rutile $(Sn_{1-x}Co_x)O_2$ thin films with x = 5-27%, and an amazingly giant magnetic moment of $(7.5\pm0.5)\mu_B$ per Co ion. High Curie temperature ferromagnetism was latterly reported for $(Sn_{1-x}Ni_x)O_2$ with x = 5% [14, 15], $(Sn_{1-x}V_x)O_2$ with x = 7% [16], $(Sn_{1-x}Cr_x)O_2$ with x = 5% [17], and $(Sn_{1-x}Fe_x)O_2$ with x = 14% [18] & x = 0.5-5% [19]. Gopinadhan et. al. [20] investigated $(Sn_{1-x}Mn_x)O_2$ (with x = 10%) thin films deposited by spray pyrolysis method and found ferromagnetic behavior above room temperature with low magnetic moment of 0.18±0.04 μ_B per Mn ion. Fitzgerald et. al. [21] studied 5% Mn-doped SnO_2 bulk ceramic samples and reported a Curie temperature of T_c = 340 K with magnetic moment of 0.11 μ_B per ordered Mn ion. On the contrary, Duan et. al. [22] reported an antiferromagnetic superexchange interaction in Mn-doped SnO_2 nanocrystalline powders and Kimura et. al. [23] observed paramagnetic behavior of Mn-doped SnO_2 thin films. Apart from this some other experiments were also carried out by various research groups on SnO_2 based dilute magnetic semiconductors and reported interesting results regarding the absence or presence of ferromagnetism [24-35]. Dilute magnetic semiconductors (DMS) based on SnO_2 could be useful for a variety of applications requiring combined optical and magnetic functionality [36]. Several devices such as spin transistors, spin light-emitting diodes, very high-density nonvolatile semiconductor memory, and optical emitters with polarized output have been proposed using $Sn_{1-x}(TM)_xO_{2-\delta}$ materials [37-40].

The origin of n-type conductivity in tin oxide semiconductor is a subject of controversy [41-43]. Thin films of pure, but non-stoichiometric, SnO_2 mostly show free-electron concentrations in the $n \sim 10^{20}$ cm^{-3} range. The existence of such high electron concentrations has historically been explained by oxygen vacancies (V_O) and tin interstitials (Sn_i) [44]. Recent density functional theory (DFT) calculations and experiments [41, 42], however, have provided evidence that usual suspects such as V_O and Sn_i are actually not responsible for n-type conductivity in majority of the cases. These calculations indicate that the oxygen vacancies are a deep donor, whereas tin interstitials are too mobile to be stable at room temperature [42]. As discussed further in this paper, hydrogen is an ubiquitous impurity that can lead to n-type doping [41, 42, 45-50].

Swift heavy ion (SHI) irradiation, in which an energetic ion beam is allowed to pass through a material, is a very effective technique to induce structural and micro-structural modifications in materials and has been used to tailor the properties of various materials including metals, insulators, semiconductors, and polymers [51-57]. High electronic energy released by the ion beams in a very short interval of time produces significant excitation of the lattice, causing changes in the structural, electrical, optical and magnetic behaviour of the materials. The SHI irradiation is known to generate controlled defects (points/clusters and columnar) and structural disorder [53, 55-57]. The parameters of ion beam such as mass and energy of the ion and the properties of the target materials such as conductivity and microstructure, play crucial role

in defect generation and engineering [52, 53, 55-57]. The ion energy and its mass, decide the magnitudes of the electronic as well as nuclear energy losses. Especially for heavy ions at high energies (i.e., for SHI), the electronic energy loss decides the type of defects as the nuclear energy loss. The other ion beam parameter, fluence, dictates the number of defects (created). The number of ion tracks per cm^2 is the same as that of fluence (ions/cm^2) because each ion creates an ion-track [53]. Modifications produced by SHI are quite different from that of low energy ions. There is a threshold of electronic energy loss, beyond which the creation of columnar defect or the latent track occurs in the materials [51, 52, 58]. This threshold energy depends on the electron-phonon coupling (g) and conductivity of the material [51, 59-61]. It can be up to about a few hundred $eV/\dot{A}$ for polymers and other insulators [61, 62] and it can be a few $keV/\dot{A}$ for metals [63-65]. There are certain materials like Ag, Cu, Ge, Si etc., in which track formation is not possible at any energy with monoatomic ion beams [66-69]. Investigations of defects produced by swift heavy ion irradiation in oxide semiconductors such as SnO_2 and In_2O_3 have become an important area of research in view of multifunctional magneto-optoelectronic devices. It would be interesting to carry out a detailed study on modifications induced by 120 MeV heavy ions on conducting tin oxide ($n \geq 10^{20} cm^{-3}$) thin films.

2. Experimental details

Thin films of $SnO_{2-\delta}$ and $Sn_{0.9}Mn_{0.1}O_{2-\delta}$ were prepared by spray pyrolyzing a mixture of aqueous solutions of tin (II) chloride di-hydrate ($SnCl_4.2H_2O$) and manganese (II) acetate tetra-hydrate ($(CH_3COO)_2Mn.4H_2O$) on glass/quartz substrates at 450^oC. The quality of these films depends on various process parameters such as spray rate, substrate temperature and the ratio of the various constituents in the solutions. Since the deviation from stoichiometry due to oxygen vacancies makes tin oxide thin films to possess semiconducting nature, it is very essential that the complete oxidation of the metal should be avoided in order to obtain films with good conductivity. This is generally achieved by adding appropriate reducing agents. Ethanol was used as the reducing agent in the present work. The substrate temperature also plays an important role in the film formation. When the substrate temperature is below 350^oC, the spray falling on the substrate will undergo incomplete thermal decomposition (oxidation) giving rise to a foggy film whose transparency as well as electrical conductivity will be very poor. If the substrate temperature is too high ($> 500^oC$) the spray gets vaporized before reaching the substrate and the film becomes almost powdery. Whereas at substrate temperature in the range of 350-500^{o}C the spray reaches the substrate surface in the semi vapor state and complete oxidation will take place to give clear SnO_2 film as a final product. Keeping these facts in mind, we have optimized substrate temperature at 450^oC.

An amount of 11.281 gm of $SnCl_4.2H_2O$ (Sigma Aldrich purity $>$ 99.99%) was dissolved in 5 ml of concentrated hydrochloric acid by heating at 90^oC for 15 mins. The addition of HCl rendered the solution transparent, mostly, due to the breakdown of the intermediate polymer molecules. The transparent solution thus obtained and subsequently diluted by ethyl alcohol, served as the precursor. To achieve Mn doping, $(CH_3COO)_2Mn.4H_2O$ was dissolved in ethyl alcohol and added to the precursor solution. The amount of $(CH_3COO)_2Mn.4H_2O$ to be added depends on the desired doping concentration. The amount of spray solution was made together 50 ml. For each concentration the reproducibility of the films were verified by repeating the experiments several times. Pyrex glass and fused quartz slides (10 mm $\times$ 10 mm $\times$ 1.1 mm), cleaned with organic solvents, were used as substrates for various studies. During deposition, the solution flow rate was maintained at 0.2 ml/min by the nebulizer (drop size 0.5-10 mm). The distance between the spray nozzle and the substrate as well as the spray time was maintained at 3.0 cm and 15 mins, respectively.

The deposited $Sn_{0.9}Mn_{0.1}O_{2-\delta}$ films were irradiated with 120 MeV Au^{9+} ions at six different fluences (1×10^{11}, 3×10^{11}, 1×10^{12}, 3×10^{12},

1×10^{13} and 3×10^{13} ions/cm^2) in a 15 MV pelletron accelerator at Inter University Accelerator Centre, New Delhi. The irradiation was performed in the direction nearly perpendicular to the sample surface. Ion beam was focused to a spot of 1 mm diameter and then scanned over 1 cm^2 area using a magnetic scanner. The vacuum of 10^{-6} Torr was maintained during irradiation experiments. During irradiation the current of the ion beam was kept at 0.5 PnA. The fluence values were measured by collecting the charge falling on the sample mounted on an electrically insulated sample holder placed in secondary electron suppressed geometry. Ladder current was integrated with a digital current integrator and the charged pulses were counted using scalar counter. A high energy of gold ions was selected so that no ions should get implanted into the parent matrix and the modifications should be limited to structural, morphological, optical, electrical and magnetic properties by high electronic energy deposition. The stopping range of the high-energy Au ions at 120 MeV is about 8.33 μm, while the electronic and nuclear stopping power are 27.79 keV/nm and 0.485 keV/nm, respectively [70, 71]. Therefore, the electronic part is dominant in our case, which is required.

The gross structure and phase purity of all films were examined by X-ray diffraction (XRD) technique using a Bruker AXS, Germany X-ray diffractometer (Model D8 Advanced) operated at 40 kV and 60 mA. In the present study, XRD data of unirradiated and irradiated thin films were collected in the scanning angle (2θ) range $20^o - 60^o$ using $Cu - K_\alpha$ radiations ($\lambda = 1.5405$ $\mathring{A}$). All the diffractograms were recorded under a slow scan with a step size of 0.01^o and a counting time of 2 s for each step, so that the presence of even small quantities of any secondary phase, if present, could be detected. The experimental peak positions were compared with the data from the database Joint Committee on Powder Diffraction Standards (JCPDS) and Miller indices were assigned to these peaks. Transmission Electron Microscopy (TEM) measurements were carried out on a JEOL USA JEM 2010 microscope with an accelerating voltage of 200 kV. All the images were digitally recorded with a slow scan charge-coupled device camera (image size 688 × 516 pixels), and image processing was carried out using the digital micrograph software. The TEM data were used for the study of grain size distribution and the crystalline character of the prepared samples. These TEM micrographs were also used to identify secondary phases present, if any, in the $Sn_{0.9}Mn_{0.1}O_{2-\delta}$ matrix. Surface morphology of the samples was analyzed by means of scanning electron microscopy using a MIRA II LMH, TESCAN: Field Emission Scanning Electron Microscope (FE-SEM) with a maximum resolution of 1.5 nm at 30 kV. Atomic Force Microscopy (AFM) was performed with Multi Mode SPM (Digital Instrument Nanoscope E) in AFM mode to examine the microstructural evolution and root mean square (rms) surface roughness of the sample before and after irradiation. Hall measurements were conducted at room temperature to estimate the film resistivity (ρ), donor concentration (n) and carrier mobility (μ) by using the four-point van der Pauw geometry employing Keithley's Hall effect card and switching the main frame system. A specially designed Hall probe on a printed circuit board (PCB) was used to fix the sample to the size 10×10 mm^2. Silver paste was employed at the four contacts. The electrical resistivity and the sheet resistance of the films were also determined using the four-point probe method with spring-loaded and equally spaced pins. The probe was connected to a Keithley voltmeter (2182A) & constant-current source (2400) system and direct current and voltage were measured by slightly touching the tips of the probe on the surface of the films. Multiple reading of current and the corresponding voltage were recorded in order to get average values. Optical absorption and transmission measurements were performed at room temperature within a wavelength range of 200-800 nm using a Cary 5000 UV-Vis spectrophotometer having spectral resolution of 0.05 nm in the UV-Vis range. As a reference, 100% baseline signals were displayed before each measurement. Magnetic measurements were carried out as a function of temperature (5 to 300 K) and magnetic field (0 to ±2 T) using a 'EverCool 7 Tesla' SQUID magnetometer. The residual field of the 7-Tesla superconducting magnet

can be reduced to < 50 mOe with ultra-low field option. Measurements were carried out on small size films placed in a clear plastic drinking straw. The data reported here were corrected for the background signal from the sample holder (clear plastic drinking straw) independent of magnetic field and temperature. Thickness of the deposited films was estimated by an Ambios surface profilometer and was approximately 500 nm.

3. Results and discussion

Ion irradiation has been considered as a useful tool for modification of the properties of films, foils and surface of bulk solids. An energetic ion that penetrates a solid loses energy mainly via two independent processes: (i) elastic collisions with target atoms (nuclear energy loss $[dE/dx]_n$) which are dominant in the low energy regime and (ii) electronic excitation and ionization (electronic energy loss, $[dE/dx]_e$) which are dominant in the high energy regime (greater than 1 MeV/nucleon). The ion energy loss per unit path length depends strongly on the ion velocity. Swift heavy ion (SHI) passes through a solid with a velocity comparable to the Bohr velocity of electrons and loses its energy in materials mainly through inelastic collisions with the atomic electrons. The rapid energy transfer during the inelastic collision results in a transient excitation of the medium that finally culminates in the production of point defects, clusters, columnar defects, and phase transformation along the path of the heavy ion beam [51-53, 72]. In the present case, we have used 120 MeV Au^{9+} ions on $Sn_{0.9}Mn_{0.1}O_{2-\delta}$ thin films. The electronic energy loss S_e, nuclear energy loss S_n and the range of ion R_p, calculated by using standard SRIM simulation program, are 27.79 keV/nm, 0.485 keV/nm and 8.33 μm, respectively [70, 71]. From the calculated values, it is clearly evident that the S_e is about two orders of magnitude more than that of S_n and the range is much larger than the film's thickness ($\sim$ 500 nm). Fig. 1 shows the variation of energy loss (both electronic and nuclear) for 120 MeV gold ions incident on $Sn_{0.9}Mn_{0.1}O_{2-\delta}$ thin film with the film thickness from the surface [70]. Near the surface of the film, S_e exceeds S_n by two orders of magnitude and is almost

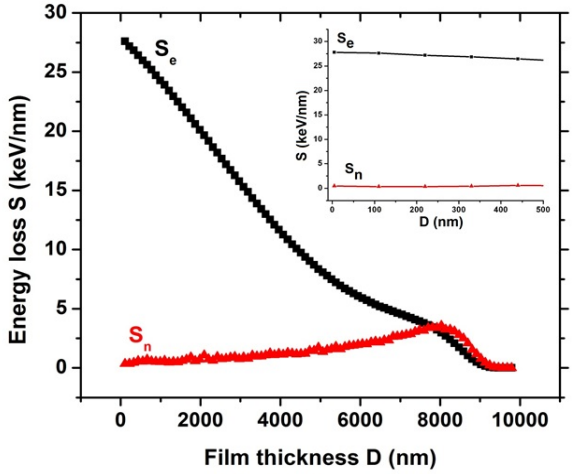

Figure 1: Variation of electronic energy loss S_e and nuclear energy loss S_n of 120 MeV Au^{9+} ions incident on $Sn_{0.9}Mn_{0.1}O_{2-\delta}$ film as a function of film thickness. The inset shows the almost constant value of S_e for even 500 nm depth from the surface of the film.

constant throughout the film thickness, as shown in the inset of Fig. 1. This reveals that the morphological and structural changes in $Sn_{0.9}Mn_{0.1}O_{2-\delta}$ thin film on irradiation by 120 MeV Au^{9+} ions are due to electronic excitations. The values of S_n, S_e and R_p for 120 MeV Au^{9+} ions in a $Sn_{0.9}Mn_{0.1}O_{2-\delta}$ thin film (thickness $\sim$ 500 nm) deposited on glass substrate (thickness ~ 1.1 μm) are mentioned in the Table 1 along with the threshold value of electronic energy loss (S_{eth}), calculated later in the paper.

3.1. Threshold energy loss

To create latent tracks or to induce amorphization in crystalline materials a certain threshold value of S_e is required and according to Szenes' [61] "thermal spike model" this threshold value S_{eth} depends on the material parameters such as electron-phonon coupling efficiency g, density ρ, melting temperature T_m, average specific heat C, irradiation temperature T_{irr}, and initial width of the thermal spike a(0). The Szenes' equation for the threshold energy can be ex-

Table 1: The values of nuclear energy loss (S_n), electronic energy loss (S_e), and range (R_p) for 120 MeV Au^{9+} ions in a $Sn_{0.9}Mn_{0.1}O_{2-\delta}$ thin film deposited on a glass substrate estimated by SRIM [70, 71]. The threshold value of electronic energy loss (S_{eth}) and possibility of track formation are also mentioned.

Parameters	$Sn_{0.9}Mn_{0.1}O_{2-\delta}$	Glass substrate
Nuclear energy loss (S_n in keV nm^{-1})	0.485	0.216
Electronic energy loss (S_e in keV nm^{-1})	27.79	14.88
Threshold electronic energy loss (S_{eth} in keV nm^{-1})	31.92	3.033
Range (μm)	8.33	15.28
Track formation	Not possible	Possible

pressed as follows:

$$S_{eth} = \frac{\pi\rho C(T_m - T_{irr})a^2(0)}{g} \quad (1)$$

The value of a(0), for semiconductors, depends on their energy band gap E_g, while for insulators it is almost constant. This ion induced thermal spike width a(0) in semiconductors can be best approximated by the expression $a(0) = b + c(E_g)^{\frac{-1}{2}}$ where b and c are constants. Using an E_g value of 4.3 eV (see Section 3.8) for $Sn_{0.9}Mn_{0.1}O_{2-\delta}$, the value of a(0) was determined from the plot of $(E_g)^{\frac{-1}{2}}$ versus a(0) as given in reference-59, and was found to be $\sim$ 6.2 nm. The electron-phonon coupling efficiency (g) can be defined as the ability of electrons to transfer their energy to the lattice. According to Szenes, the value of g depends on electron concentration (n). It is found that, for conductive materials (n $\geq 10^{20}$ cm^{-3}), the value of g is $\sim$ 0.092 [59], while for insulators it is $\sim$ 0.4 [73]. In a later section-3.6, we have reported the results of electrical measurements. From these measurements we can say as-deposited $Sn_{0.9}Mn_{0.1}O_{2-\delta}$ samples are in conducting state with n = 1.93×10^{20} cm^{-3}. By substituting the values of $\rho = 6.99$ g/cm^3, T_m = 1898 K, T_{irr} = 300 K, and C = 0.349 J/(gK) [74, 75] in equation-1, one can obtain $S_{eth} = 31.92$ keV/nm for $Sn_{0.9}Mn_{0.1}O_{2-\delta}$. For the present case of 120 MeV Au^{9+} ions irradiating the $Sn_{0.9}Mn_{0.1}O_{2-\delta}$ film, S_e is 27.79 keV/nm (see table-1), which is less than the threshold value (S_{eth} = 31.92 keV/nm) required to produce tracks/melted zones. Therefore we expect that only point defects or clusters of point defects will produce in $Sn_{0.9}Mn_{0.1}O_{2-\delta}$ film after irradiation. On the other hand, for glass substrate, the value of S_{eth} is 3.033 keV/nm (calculated by using $\rho = 2.53$ g/cm^3, a(0) = 4.5 nm, C = 0.88 J/(gK), T_m = 1673 K, T_{irr} = 300 K, g = 0.4), which is lower than the available S_e of 14.88 keV/nm induced by 120 MeV Au^{9+} ions. Hence, track formation is only possible in the glass substrate but not in the $Sn_{0.9}Mn_{0.1}O_{2-\delta}$ film. This discontinuity in track formation can induce stress at the $Sn_{0.9}Mn_{0.1}O_{2-\delta}$/glass substrate interface.

It is important to understand that the way in which the huge energy ($S_e \sim$ 27.79 keV/nm) is deposited to the system will modify the materials. The swift heavy ion initially interacts with the atomic electrons (electronic subsystem) of the target material and transfers its energy to electrons (valence and core electrons) in a time less than 10^{-16} s. Since timescale of electron-ion interaction is very small, that's why initially the lattice (atomic subsystem) of target material does not respond in that timescale [51, 52]. The transfer of the excess heat energy of the excited electronic subsystem to the atomic subsystem may lead to an increase in the local temperature of the target material and therefore a high energy region is developed in the close vicinity

of the ion path. The amount of energy transferred (locally) depends on the coupling between the electronic and atomic subsystems. This coupling is known as electron-phonon coupling (g) and it can be defined as the ability of electrons to transfer their energy to the lattice. According to Szenes, the value of g depends on the carrier concentration (n) in the target material. It is found that, for conductive materials ($n \geq 10^{20} cm^{-3}$), the value of g is ~ 0.092 [59], while for insulators it is ~ 0.4 [73]. The amorphized latent tracks are created only above a certain threshold value of S_e, which inversely depends on the electron-phonon coupling efficiency (g). Therefore, conductive targets will require very high beam energy to create latent tracks/melted zones. But if $S_e < S_{eth}$, then only point defects or cluster of point defects will create in target material after irradiation. A point to note here is that in insulator if $S_e < S_{eth}$ then point defects will create locally around the ion path whereas in conductive material these defects will create uniformly through out the material. In this way, we can conjecture that the SHI irradiation can create tracks or point defects depending upon the initial state of the material. But if the system already contains such defects, then they can be annealed through the irradiation.

3.2. Equilibrium substrate/film temperature

The input power density can be calculated by using the following equation:-

$$P = \frac{(Irradiation\ Energy \times Beam\ Current)}{Scanning\ Area}$$

In the present case the maximum input power density is

$$P = \frac{(120\ MeV \times 4.5\ nA)}{1\ cm^2} = 0.54 \frac{W}{cm^2}$$

The power of the ion beam deposited in the target can be removed mainly by thermal radiation and directed to the heat sink constituted by the vacuum chamber. During irradiation the samples were attached to a massive sample holder using a double sided tape. Although the actual sample holder structures including the target chamber are complicated, but we have used the simplified Stefan's equation [76, 77] for temperature determination,

$$P = \epsilon\sigma(T^4 - T_s^4), \tag{2}$$

where P is the input power density of high energy ion beam, σ is the Stefan-Boltzmann constant of 5.67 $\times\ 10^{-12}\ \frac{W}{cm^2 K^4}$, ϵ is the effective emittance of the glass substrate, T_s is the surrounding target chamber temperature ($\sim$ 300 K), and T is the equilibrium substrate/film temperature. The effective emittance of target/substrate can be determined by substitution of experimentally measured temperature in above equation. Thus, effective emittance (ϵ) was found to 0.3 for silicon wafer [76]. In the present study, we have used the glass substrates therefore the effective emittance (ϵ) is kept little lesser ($\epsilon = 0.2$) than that used for silicon ($\epsilon = 0.3$). This is because of the fact that the crystalline silicon substrate may dissipate more input power in terms of radiation than that of amorphous glass substrate [78, 79]. By using the values of input power density (P = 0.54 W/cm^2) and effective emittance ($\epsilon = 0.2$) in above equation [Eq. (2)], the equilibrium temperature is estimated to $\sim$ 834 K for $Sn_{0.9}Mn_{0.1}O_{2-\delta}$ film/glass substrate. This calculated equilibrium temperature is higher than the crystallization temperature of SnO_2 [74, 80] and expected to be develop within the grains of material during irradiation and facilitate (i) increase of grain size (judged by AFM), (ii) removal of micro-strain (evidenced by XRD measurements), and (iii) migration of point defects (explained by XRD and electrical measurements).

The increase rate of the glass substrate temperature during irradiation can be deduced by using the following equation:

$$\frac{dT}{dt} = \frac{[P - \epsilon\sigma(T^4 - T_s^4)]}{\rho w C}, \tag{3}$$

where C is the heat capacity, ρ is the glass substrate density, and w is the substrate thickness.

Eq. (3) can be solved by separation of variable technique as follows:

$$dt = \frac{dT}{a(T^4 - b)}, \tag{4}$$

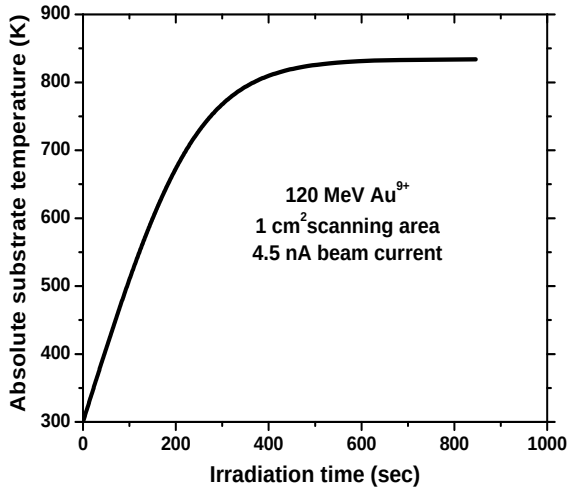

Figure 2: The transient substrate/film temperature calculated by using an input power density of 0.54 $\frac{W}{cm^2}$.

where a = $\frac{-\epsilon\sigma}{\rho wC}$ = -4.6304×10^{-12} $K^{-3}s^{-1}$ and b = $\frac{P}{\epsilon\sigma} + T_s^4$ = 4.8429×10^{11} K^4.

The differential Eq. (4) can be numerically solved (by Wolfram language [81]) as follows:

t = c_1 - 93.002 ln (834.212 - T) + 93.002 ln (T + 834.212) + 186.004 tan^{-1} (1.199 × 10^{-3}T)

Apply initial condition: T = 300 K at t = 0.

t = -93.002 ln (834.212 - T) + 93.002 ln (T + 834.212)

+ 186.004 $\tan^{-1}$ (1.199 × 10^{-3} T) − 134.234 (5)

The calculated results of Eq. (5) are shown in Fig. 2. In this calculation, the glass substrate thickness (w), effective emittance (ϵ), target material density (ρ), target heat capacity (C), and surrounding target temperature (T_s) are assumed to be 0.11 cm, 0.2, 2.53 g/cm^3, 0.88 J/gK, and 300 K, respectively. As clearly seen from Fig. 2, the glass substrate temperature reaches its equilibrium value (∼ 834 K) in several hundred seconds. The irradiation fluences in the present experiment were in the range of 1×10^{11} - 3×10^{13} $ions/cm^2$, which means that the irradiation periods were in the range of 32-9600 sec when 1 cm^2 sample was used. In the case of high fluence ($\geq 3 \times 10^{12}$ $ions/cm^2$), irradiation period is much longer than the amount of time needed to achieve equilibrium temperature. Therefore, in this case, the samples spend their almost full irradiation period at equilibrium temperature. This equilibrium temperature can influence the physical properties of samples irradiated with high fluence.

3.3. Brief review on the properties of point defects in SnO_2

First-principles calculations for point defects in SnO_2, based on density functional theory (DFT) and the local density approximation (LDA) or the generalized gradient approximation (GGA), have been reported by several groups [41,44,45, 82-91]. Relying on calculations based purely on DFT-LDA approach, Kilic and Zunger [44] concluded that oxygen vacancies (V_O) and tin interstitials (Sn_i) are the cause of the frequently observed unintentional n-type conductivity in SnO_2. For non-stoichiometric SnO_2 they [44] suggested that thermodynamic transition levels for oxygen vacancies lie at just 114 meV below the conduction band minimum ($\epsilon_{V_O}(2+/0) = E_{CBM}$ - 114 meV) and thus can be readily thermally ionized. For tin interstitials a transition level 203 meV above the conduction band minimum ($\epsilon_{Sn_i}(4+/3+) = E_{CBM}$ + 203 meV) was found, implying a spontaneous donation of electrons into the conduction band (CB). However, calculations based purely on LDA or GGA functionals suffer from the band-gap error [42, 82, 92-96]. In the case of SnO_2, the calculated band gap using LDA functional is only 1.16 eV, compared to the experimental value of 3.6 eV [42]. This underestimation of the band gap in DFT-LDA/GGA based calculations leads to large uncertainties in the calculated position of the defect-induced states in the band gap. If these defect-induced states are occupied with electrons, the formation energy of defect also reflects these errors. Several approaches have been developed to overcome DFT-LDA/GGA deficiencies in predicting band gap of SnO_2 semiconductor. These

Table 2: Summary of the irradiation conditions: beam fluence, beam current, irradiation period, and temperature of irradiation.

Beam fluence ($ions/cm^2$)	Beam current (nA)	Irradiation period (sec)	Substrate/film temperature during irradiation (K)
1×10^{11}	4.5	32	Low temperature transient condition
3×10^{11}	4.5	96	Low temperature transient condition
1×10^{12}	4.5	320	Low temperature transient condition
3×10^{12}	4.5	960	$\sim$ 834 K (not entire time)
1×10^{13}	4.5	3200	$\sim$ 834 K (almost entire time)
3×10^{13}	4.5	9600	$\sim$ 834 K (almost entire time)

Table 3: Properties of native or intrinsic defects in n-type SnO_2 (oxygen poor condition) [41, 42, 44-50, 82, 83, 85, 92-98, 106-146].

Defect	Character	Formation energy (Transition level)	Migration energy/temperature	Formation probability in pristine samples	Formation probability in irradiated samples	Effect on lattice
V_O^{2+}	Donor	Stable in p-type	Very high	-	-	Expansion
V_O^{1+}	Donor	Unstable for all E_F	-	-	-	-
V_O^{0}	Neutral	Modest (Deep $\sim$ 1.8 eV)	Very high ($\approx 900K$)	Modest	Very high	Contraction
Sn_i^{4+}	Donor	Very high $\sim$ 12 eV (Shallow)	Low $\sim$ 0.43 eV	Very low	Very low	Expansion
Sn_i^{3+}	Donor	Unstable	-	-	-	-
Sn_i^{2+}	Donor	Unstable	-	-	-	-
Sn_O^{4+}	Donor	Very high (Shallow)	High ($\approx 500K$)	Very low	High	Expansion
O_i^{2-}	Acceptor	High (Deep)	Modest ($< 500K$)	Low	High	Expansion
V_{Sn}^{4-}	Acceptor	Modest in n-type (Deep)	High ($\approx 500K$)	Modest (Very low @ $T > 500K$)	Very high	Expansion
O_{Sn}^{2-}	Acceptor	Very high (Deep)	High ($\approx 500K$)	Very low	High	Contraction
H_i^{1+}	Donor	Low (Shallow)	Low $\sim$ 0.57 eV	Very low at room temperature	-	-
H_O^{1+}	Donor	Low (Shallow)	Very high $\sim$ 2.2 eV	Very high	-	Expansion

include (1) LDA + U approach, (2) HSE screened hybrid functional, (3) self-interaction corrections, and (4) Green-function-based quasi particle method [41, 42, 82-85, 92-105]. Using LDA + U approach, Singh et. al. [42] carried out calculations for SnO_2. Their results indicate that oxygen vacancy is a deep donor with a transition level $\epsilon_{V_O}(2+/0)$ about 1.8 eV below the CB edge i.e. V_O is stable in the neutral charge state in n-type SnO_2. Therefore, it is clear that V_O cannot provide electrons to the CB by thermal excitation in steady state, and therefore it cannot be a source of the frequently observed unintentional n-type conductivity. For V_O^0, the three nearest-neighbors Sn atoms are displaced inward by 2.5%, whereas for V_O^+ and V_O^{2+}, the relaxations are outward by 5.6% and 10% of the equilibrium Sn-O bond length, respectively. In addition, they [42] found that other native point defects, e.g., Sn interstitials and Sn antisites, are also unlikely sources of conductivity due to their high formation energies. Recent first-principle calculations have drawn attention on the role of donor impurities in unintentional n-type conductivity [41, 42, 82, 92, 93]. Among the possible impurities, hydrogen stands out as a prime candidate [41, 42, 45-50, 82, 92, 93]. In both forms, substitutional and interstitial, hydrogen has been predicted to act as a shallow donor in n-type SnO_2 [42]. But by means of density functional calculations, it is found that interstitial hydrogen (H_i) is highly mobile and can easily diffuse out of the SnO_2 samples. The migration barrier of interstitial hydrogen is only 0.57 eV. This low barrier value makes it difficult to explain the stability of the n-type conductivity at relatively high temperature. On the other hand substitutional hydrogen (H_O) species is much more thermally stable than interstitial hydrogen and can explain stability of n-type conductivity at high temperature and its variation with partial pressure of oxygen in annealing environments. The substitutional hydrogen has low formation energy and occurs exclusively in the positive charge state H_O^+ [42]. Hydrogen is by no means the only possible shallow donor impurity in tin oxide, but it is a very likely candidate for an impurity that can be unintentionally incorporated and can explain observed unintentional n-type conductivity [82]. Several groups have reported on the incorporation of hydrogen in tin oxide and many have claimed that hydrogen substitutes for oxygen [41, 42, 45-50, 82, 92, 93, 106-122]. Table 3 lists the details of all native point defects and hydrogen impurities, based on several reported results [41, 42, 44-50, 82, 83, 85, 92-98, 106-146]. These summarized results will help us later to interpret experimental data in this research paper.

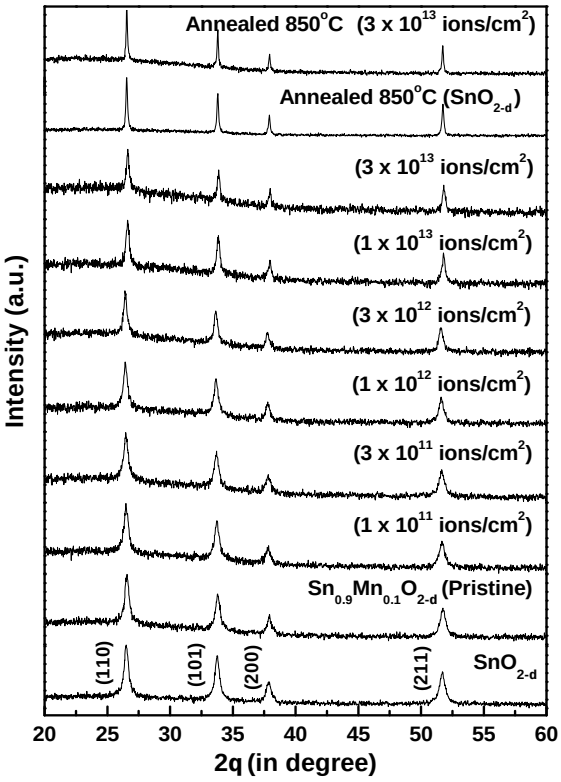

Figure 3: X-ray diffraction patterns of unirradiated, irradiated and annealed thin films.

3.4. X-ray diffraction studies

Fig. 3 displays the X-ray diffraction patterns of unirradiated ($SnO_{2-\delta}$ and $Sn_{0.9}Mn_{0.1}O_{2-\delta}$), irradiated ($1 \times 10^{11}$ - 3×10^{13} $ions/cm^2$) and annealed ($SnO_{2-\delta}$ and 3×10^{13} $ions/cm^2$) samples. From the analysis of X-ray diffraction patterns, it is evident that only the peaks corresponding to the rutile-type SnO_2 phase (space group $P4_2/mnm$) are detected

Table 4: Summary of various results obtained through analysis of XRD patterns.

Samples	Lattice parameters		Cell volume	Defects present	Defects
	a = b ($\dot{A}$)	c ($\dot{A}$)	($\dot{A}^3$)	in the samples	annealed/migrated
$SnO_{2-\delta}$	4.7491	3.1998	72.1681	H_O^+	V_{Sn}^{4-}
$Sn_{0.9}Mn_{0.1}O_{2-\delta}$ (Pristine)	4.7413	3.1967	71.8616	H_O^+	V_{Sn}^{4-}
1×10^{11} $ions/cm^2$	4.7521	3.2016	72.3000	H_O^+ (Partially Present) $V_{Sn}^{4-} > V_O^0 > O_i^{2-} > Sn_O^{4+} > O_{Sn}^{2-}$	H_O^+ (Partially Annealed), Sn_i^{4+}
3×10^{11} $ions/cm^2$	4.7551	3.2034	72.4320	H_O^+ (Partially Present) $V_{Sn}^{4-} > V_O^0 > O_i^{2-} > Sn_O^{4+} > O_{Sn}^{2-}$	H_O^+ (Partially Annealed), Sn_i^{4+}
1×10^{12} $ions/cm^2$	4.7611	3.2069	72.6942	H_O^+ (Partially Present) $V_{Sn}^{4-} > V_O^0 > O_i^{2-} > Sn_O^{4+} > O_{Sn}^{2-}$	H_O^+ (Partially Annealed), Sn_i^{4+}
3×10^{12} $ions/cm^2$	4.7641	3.2087	72.8267	H_O^+ (Partially Present) $V_{Sn}^{4-} > V_O^0 > O_i^{2-} > Sn_O^{4+} > O_{Sn}^{2-}$	H_O^+ (Partially Annealed), Sn_i^{4+}
1×10^{13} $ions/cm^2$	4.7354	3.1905	71.5438	V_O^0	$H_O^+, Sn_i^{4+}, O_i^{2-}$, $Sn_O^{4+}, O_{Sn}^{2-}, V_{Sn}^{4-}$
3×10^{13} $ions/cm^2$	4.7324	3.1887	71.4129	V_O^0	$H_O^+, Sn_i^{4+}, O_i^{2-}$, $Sn_O^{4+}, O_{Sn}^{2-}, V_{Sn}^{4-}$
Annealed 850^oC ($SnO_{2-\delta}$)	4.7431	3.1935	71.8442	-	$H_O^+, Sn_i^{4+}, O_i^{2-}, Sn_O^{4+}$, $O_{Sn}^{2-}, V_{Sn}^{4-}, V_O^0$
Annealed 850^oC (3×10^{13})	4.7437	3.1933	71.8578	-	$H_O^+, Sn_i^{4+}, O_i^{2-}, Sn_O^{4+}$, $O_{Sn}^{2-}, V_{Sn}^{4-}, V_O^0$

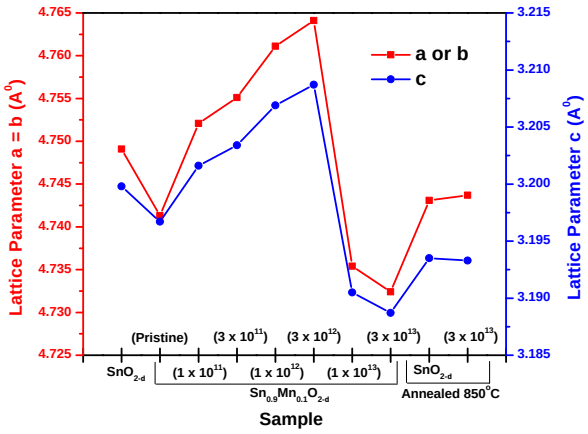

Figure 4: Changes in the lattice parameters a and c of respective samples. Here x-axis is not scaled for better clarity.

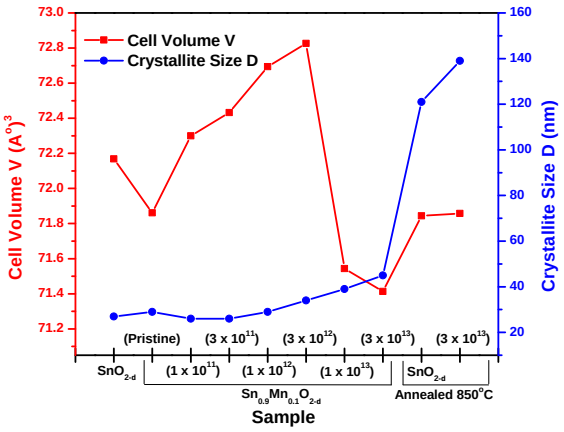

Figure 5: Changes in the cell volume (V) and crystallite size (D) of respective samples. Here x-axis is not scaled for better clarity.

in all samples. No additional reflection peaks related to impurities, such as unreacted manganese metal, oxides or any other tin manganese phases are detected. The lack of any impurity phases shows that the Mn is evenly distributed throughout the SnO_2. The lattice parameters (a and c) and cell volume (V) are calculated by using the (110), (101) and (200) reflection planes in the XRD patterns (see Figs. 4 & 5). The complete structural analyses of the samples are given in the Table 4. The observed contraction in cell volume from 72.1681 $\mathring{A}^3$ to 71.8616 $\mathring{A}^3$ on Mn doping, indicating the replacement of Sn^{4+} by Mn^{3+}. The lattice parameter a is observed to decreases from 4.7491 $\mathring{A}$ to 4.7413 $\mathring{A}$, while the lattice parameter c decreases from 3.1998 $\mathring{A}$ to 3.1967 $\mathring{A}$. These results are in agreement with the fact that the difference in the ionic radius of Mn^{3+} (0.58 $\mathring{A}$) and Sn^{4+} (0.69 $\mathring{A}$) is rather small, leading to very small changes in the lattice constants on doping with Mn. For Mn, there are three oxidation states namely Mn^{4+} (0.53 $\mathring{A}$), Mn^{3+} (0.58 $\mathring{A}$) and Mn^{2+} (0.82 $\mathring{A}$) [147]. The ionic radius of each ion in $\mathring{A}$ is given in brackets. But the magnitude of cell volume change indicates that the valence of the Mn ion is most probably +3 instead of +2 or +4. This speculation also finds support from the studies performed on oxides of manganese showing that in its oxides, Mn^{3+} prefers to be in an octahedral coordination [148], just like Sn^{4+} in the rutile-type structure of tin oxide (SnO_2). It is clear from Fig. 6 that Mn substitution effects the intensity of SnO_2 peaks. As we know, the intensity of the scattered radiation is related to structure factor and this factor is determined by the presence of bound electrons in an atom. Since Mn has less bound electrons than Sn that's why the substitution of Sn by Mn in the SnO_2 lattice should yield a structure factor, which is almost half the value for Sn. If there is any change in the occupation site of Mn, i.e., substitutional to interstitial, the same may be reflected as an increase in the structure factor.

In this article, we have assumed annealed samples as defect-free samples (see Fig. 7). As we know, the migration temperatures of almost all point defects are less than 700^{o}C (see Table-3). Therefore, samples which have been annealed at a temperature of 850^{o}C, they may be free of defects. After careful analysis of XRD patterns, we found that the unit cell volume of as-deposited SnO_2 thin film is slightly more than that of defect free annealed SnO_2 thin film (see Fig. 7). This increase in cell volume may

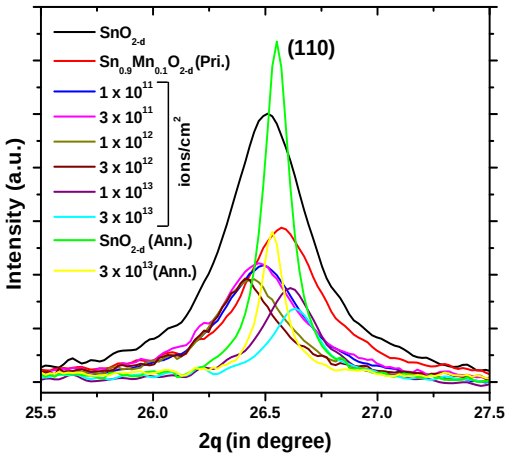

Figure 6: Changes in the (110) cassiterite peak position and intensity of respective samples.

be due to presence of expansion-type point defects such as H_O^+, V_{Sn}^{4-}, O_i^{2-}, Sn_O^{4+}, Sn_i^{4+}. Among all these expansion-type point defects only H_O^+ and V_{Sn}^{4-} may be responsible for the observed increase in cell volume, because as we know, the formation energies of other expansion-type defects such as O_i^{2-}, Sn_O^{4+}, Sn_i^{4+} are very high as compared to formation energies of H_O^+ and V_{Sn}^{4-} [41, 42, 82, 92, 93]. It is impossible to create such defects of high formation energies through thermodynamic/equilibrium process. The direct and unambiguous method for introducing such defects in lattice is by high-energy ion beam irradiation. As we know, tin vacancies are acceptor type point defects and play a lead role in conductivity killing (see Table-3). That's why we have prepared thin films at a temperature of 450^oC, which is somewhere in between the migration temperature of tin vacancy and substitutional hydrogen. Thus, we can conclude that the slight expansion observed in cell volume of pure SnO_2 thin film is only due to H_O^+ point defects. According to Singh et. al. [42], V_O^0 defect is a contraction type, but when hydrogen does occupy the oxygen vacancy site (V_O^0) then resultant defect H_O^+ becomes expansion type, because after hydrogen substitution the resultant Sn-H bond length (2.14 $\mathring{A}$) is slightly more than Sn-O bond length (2.07 $\mathring{A}$). In a later section-3.6, we have reported the results of electrical measurements. From these measurements we can say carrier concentration of as prepared pure SnO_2 thin film is very high. According to Singh et. al. & Janotti et. al. [42, 82, 92, 93] H_O^+ is also stables enough to explain this observed high unintentional n-type conductivity.

The effect of swift heavy ion irradiation on the structural parameters of the $Sn_{0.9}Mn_{0.1}O_{2-\delta}$ thin films as determined by XRD analysis is now discussed. The swift heavy ion irradiation is a very effective technique to create point defects in the target material. Both expansion (V_{Sn}^{4-}, O_i^{2-}, Sn_O^{4+}) and contraction (V_O^0, O_{Sn}^{2-}) type of native defects can be created with the help of ion beam. These defects are created in accordance with its respective formation energy; those having less formation energy are created in large number and vice-versa. SHI irradiation can also anneal-out the defects via two ways: self-annealing and beam heating. Self-annealing is a process through which pre-existing defects of pristine sample are annealed-out. In this process, ion-energy transfer through electron-phonon coupling makes the target abnormally excited and the region around the ion track gets suddenly heated to a very high temperature within small time period. This self-annealing of pre-existing defects depends upon the ion fluence of irradiation. Almost all pre-existing defects may anneal-out at high fluence irradiation. On the other hand, the ion beam heating process is based on the heat produced by the transfer of beam power. The power of the ion beam warms up the target to a certain equilibrium temperature in specific period of time (see Section - 3.2). In the case of high fluence, irradiation period is much longer than the amount of time needed to achieve equilibrium temperature. Therefore, in this case those defects cannot be generated permanently by irradiation whose migration temperature is less than equilibrium temperature. The cell volumes estimated for pristine, 1×10^{11}, 3×10^{11}, 1×10^{12}, 3×10^{12}, 1×10^{13}, 3×10^{13} $ions/cm^2$ irradiated films are

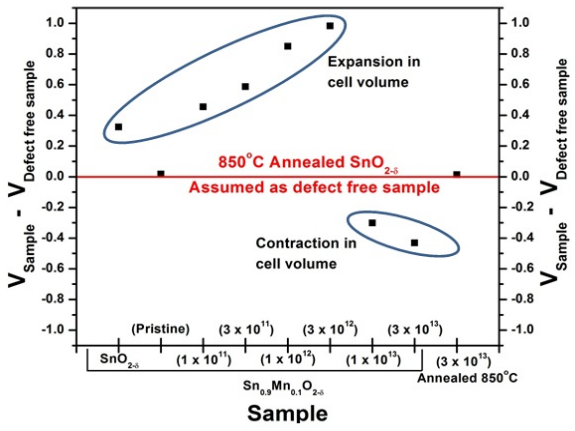

Figure 7: Deviations in cell volume of all samples with respect to defect free sample.

71.8616, 72.3000, 72.4320, 72.6942, 72.8267, 71.5438 and 71.4129 $\mathring{A}^3$, respectively. The irradiated samples should show a reduction in the unit cell volume due to self-annealing of pre-existing expansion-type H_O^+ defects. But here, instead of decrease in cell volume, an increase has been observed upto 3×10^{12} $ions/cm^2$ (see Fig. 7). In spite of self-annealing, ion beam can also generate defects in accordance with its formation energy. As we know, the expansion-type V_{Sn}^{4-} defects have lowest formation energy among the all native point defects (V_{Sn}^{4-}, V_O^0, O_i^{2-}, Sn_O^{4+}, O_{Sn}^{2-}) under n-type conditions. Therefore, after irradiation, they may be present in large numbers as compared to other native defects and can explain the observed increase in cell volume. After the irradiation fluence of 3×10^{12} $ions/cm^2$, we have observed a decrease in the cell volumes of samples (see Fig. 7). This decrease in the cell volumes can be explained in terms of ion beam heating phenomena. In case of high fluence (such as 1×10^{13} or 3×10^{13} $ions/cm^2$), material spends almost entire time during irradiation at equilibrium temperature ($\sim$ 834 K). So possibly in such case, those point defects cannot be created permanently through irradiation whose migration temperature is less than equilibrium temperature. Among the all possible defects (V_{Sn}^{4-}, V_O^0, O_i^{2-}, Sn_O^{4+}, O_{Sn}^{2-}) only contraction-type V_O^0 defect has greater migration temperature ($\sim$ 900 K) than equilibrium substrate/film temperature ($\sim$ 834 K) [42, 82, 92, 93]. Therefore, only contraction-type V_O^0 defects may be present in high fluence irradiated samples and can explain the observed contraction in cell volume. We have also analyzed the effect of annealing on the cell volumes of irradiated and pure SnO_2 samples. It should be noted that the cell volumes of both annealed films (irradiated at 3×10^{13} $ions/cm^2$ and pure SnO_2) are almost equal. This observation confirms the creation of point defects in irradiated materials. If we keep annealing temperature of irradiated samples higher than the migration temperature of all possible defects (approximately 700^o) then all defects present in the irradiated samples becomes migrate and consequently samples acquire defect free state.

3.5. Texture coefficient, crystallite size, micro and macro-strain

The preferential orientation of the crystallites in the films was studied by calculating the texture coefficient C(hkl) of each XRD peak using the equation [149, 150]:

$$C(hkl) = \frac{N(I(hkl)/I_o(hkl))}{\sum(I(hkl)/I_o(hkl))} \tag{6}$$

where $C(hkl)$ is the texture coefficient of the plane (hkl), I(hkl) is the measured integral intensity, $I_o(hkl)$ is the JCPDS standard integral intensity for the corresponding powder diffraction peak (hkl), and N is the number of reflections observed in the x-ray diffraction pattern. C(hkl) is unity for each XRD peak in the case of a randomly oriented film and values of C(hkl) greater than unity indicate preferred orientation of the crystallites in that particular direction. The degree of preferred orientation σ of the film as a whole can be evaluated by estimating the standard deviation of all the calculated C(hkl) values [151]:

$$\sigma = \sqrt{\frac{\sum[C(hkl) - C_o(hkl)]^2}{N}} \tag{7}$$

where $C_o(hkl)$ is the texture coefficient of the powder sample which is always unity. The zero value of σ

Table 5: The Texture coefficient C(hkl), the degree of preferential orientation σ, crystallite size, non-uniform and uniform strain for all the samples.

Samples	Texture coefficient C(hkl)				σ	Crystallite Size (nm)	Non-Uniform Strain	Uniform Strain	
	(110)	(101)	(200)	(211)				a - direction	c - direction
$SnO_{2-\delta}$	0.792	0.865	1.442	0.901	0.258	27	12.5×10^{-4}	1.265×10^{-3}	1.973×10^{-3}
$Sn_{0.9}Mn_{0.1}O_{2-\delta}$ (Pristine)	0.814	0.783	1.504	0.899	0.294	29	12.7×10^{-4}	-0.379×10^{-3}	1.002×10^{-3}
1×10^{11} $ions/cm^2$	0.844	0.826	1.498	0.833	0.287	26	11.4×10^{-4}	1.897×10^{-3}	2.536×10^{-3}
3×10^{11} $ions/cm^2$	0.827	0.824	1.476	0.873	0.276	26	10.8×10^{-4}	2.529×10^{-3}	3.100×10^{-3}
1×10^{12} $ions/cm^2$	0.820	0.812	1.515	0.853	0.298	29	8.71×10^{-4}	3.795×10^{-3}	4.196×10^{-3}
3×10^{12} $ions/cm^2$	0.850	0.816	1.480	0.855	0.277	34	6.24×10^{-4}	4.427×10^{-3}	4.759×10^{-3}
1×10^{13} $ions/cm^2$	0.743	0.813	1.473	0.972	0.285	39	3.77×10^{-4}	-1.623×10^{-3}	-0.939×10^{-3}
3×10^{13} $ions/cm^2$	0.739	0.719	1.622	0.920	0.367	45	1.15×10^{-4}	-2.256×10^{-3}	-1.503×10^{-3}
Annealed 850^oC $(SnO_{2-\delta})$	0.828	0.795	1.460	0.916	0.269	121	2.51×10^{-4}	-	-
Annealed 850^oC (3×10^{13})	0.849	0.839	1.424	0.887	0.246	139	0.49×10^{-4}	0.126×10^{-3}	-0.062×10^{-3}

indicates that the crystallites in the film are oriented randomly. The higher value of σ indicates that the crystallites in the film are oriented preferentially [151]. The texture coefficient C(hkl) of all the XRD peaks along with the value of σ for each film is given in Table 5. It can be seen that the plane (200) has a high texture coefficient for all the films. The thin film attains maximum preferential orientation ($\sigma = 0.367$) when the fluence value is 3×10^{13} $ions/cm^2$. However, it should be highlighted that none of the films possess a significant preferential orientation since the value of σ is less than unity for all the films.

This section also deals with the determination of crystallite size, non-uniform (micro) and uniform (macro) strain by XRD peak broadening measurements. Crystallite size is a measure of the size of coherently diffracting domains and lattice strain is a measure of the distribution of lattice constants arising from lattice defects. In polycrystalline materials, two types of lattice strain can be encountered: uniform strain (macro-strain) and non-uniform strain (micro-strain). Uniform strain causes the unit cell to contract/expand in an isotropic way. This simply leads to a change in the lattice parameters and shift of the diffraction peaks. There is no peak broadening associated with this type of lattice strain. Moreover, non-uniform strain leads to systematic shifts of atoms from their ideal positions and to peak broadening [152, 153]. The effect of both micro- and macro-strain on the fundamental Bragg reflection peak is illustrated in Fig. 8. A portion of an unstrained crystallite appears in panel (a) on the left, and the set of transverse reflecting planes shown has everywhere its equilibrium spacing d_0. The Bragg diffraction peak from these reflecting planes appears on the right. If the crystallite is then given a uniform tensile strain at right angles to the reflecting planes, their spacing becomes larger than d_0 and the corresponding Bragg diffraction peak shifts to lower angles but does not otherwise

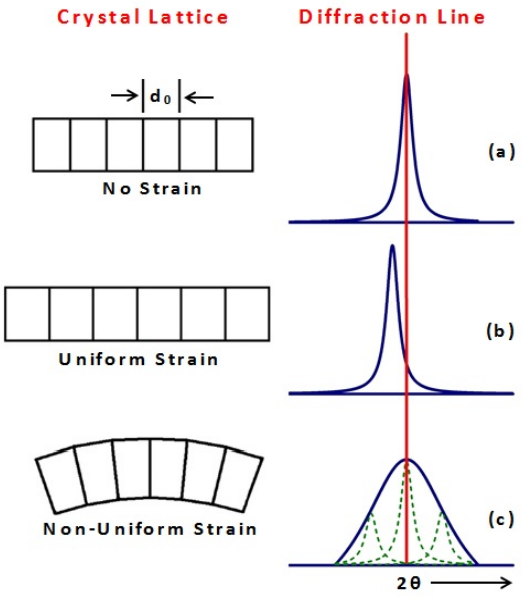

Figure 8: A portion of an unstrained grain appears in (a), uniform tensile strain (b) and non-uniform strain (c). According to the figure the uniform strain affect the peak position and the non-uniform strain affect the peak broadening and intensity.

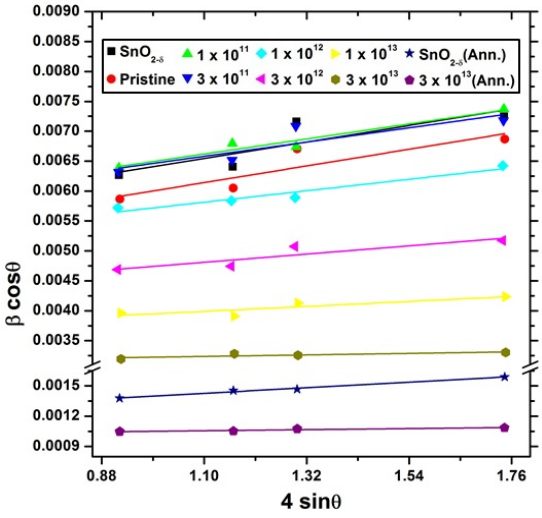

Figure 9: Williamson-Hall plots of all samples.

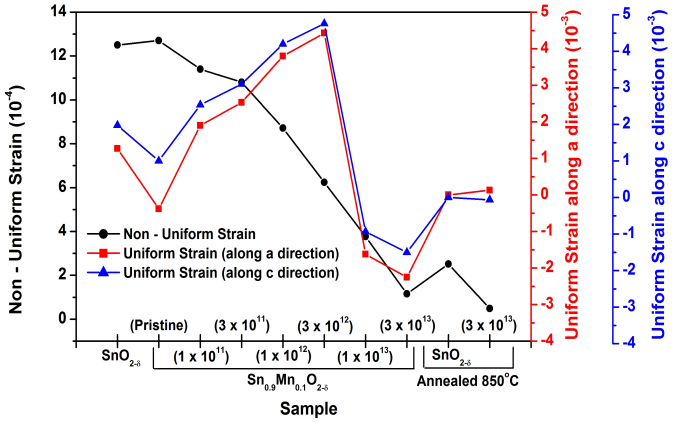

Figure 10: Changes in the non-uniform and uniform strain of respective samples. Here x-axis is not scaled for better clarity.

change, as shown in panel (b). This peak shift is the basis of the x-ray method for the measurement of macro-strain. In panel (c) the crystallite is bent and the strain is non-uniform; on the top (tension) side the reflecting plane spacing exceeds d_0 , on the bottom (compression) side it is less than d_0, and somewhere in between it equals d_0 . One can imagine this crystallite to be composed of a number of small regions in each of which the reflecting plane spacing is substantially constant but different from the spacing in adjoining regions. These small regions cause the various sharp diffraction peaks indicated on the right of panel (c) by the dotted curves. The sum of these sharp diffraction peaks, each slightly displaced from the other, is the broadened diffraction peak shown by the full solid curve and, of course, the broadened diffraction peak is the only one experimentally observable [154]. In the case of nanocrystalline materials where crystallite size also plays a role in peak broadening the two effects strain and size broadening overlap each other. In such cases the micro-strain or crystallite size can only be determined by separating the two effects. However, the peak width derived from micro-strain varies as $\tan\theta$, whereas crystallite size varies as $1/\cos\theta$. This difference in behaviour as a function

of 2θ enables one to discriminate between the strain and size effects on peak broadening. The peak width contribution from crystallite size is inversely proportional to the crystallite size [155]. Williamson-Hall (W-H) analysis is a simplified integral breadth method where micro-strain-induced and crystallite size-induced broadening are de-convoluted by considering the peak width as a function of 2θ [156-158]. Williamson and Hall assumed that both strain and size broadened profiles are Lorentzian [157]. Based on this assumption a mathematical relation was established between the integral breadth (β), the lattice micro-strain (ε) and volume weighted average crystallite size (D) as follows:

$$\beta \cos\theta = \frac{k\lambda}{D} + 4\varepsilon \sin\theta \tag{8}$$

Where k is a constant equal to 0.94, λ is the wavelength of the radiation (1.54056 $\mathring{A}$ for CuK_α radiation), and θ is the peak position. The instrumental resolution in the scattering angle 2θ, β_{inst}, was determined by means of a standard crystalline silicon sample and approximated by

$$\beta_{inst} = 9 \times 10^{-6}\ (2\theta)^2 \text{ - } 0.0005\ (2\theta) + 0.0623$$

Finally, the integral breadth β without instrumental contribution was obtained according to the relation:

$$\beta = \beta_{measured} - \beta_{instrumental} \tag{9}$$

Eq. 8 represents the general form of a straight line $y = mx + c$. The plot between $\beta\cos\theta$ and $4\sin\theta$ gives a straight line having slope ε and intercept $k\lambda/D$. The values of crystallite size and micro-strain can be obtained from the inverse of intercept and the slope of the straight line, respectively. The Williamson-Hall plots for all the samples are given in Fig. 9 and the results extracted from these plots are listed in Table 5. These results illustrate the influence of the ion irradiation and thermal annealing on the crystallite size and the micro-strain of the samples. Although W-H analysis is an averaging method apart from TEM imaging, it still holds a dominant position in crystallite size determination. It is clear from intercept values that SHI irradiation does not influence the crystallite size much in the low fluence regime, but causes a significant increase at the fluence of 1×10^{13} and 3×10^{13} $ions/cm^2$. The crystallite size of the pristine film changes from 29 nm to 45 nm on irradiation at the fluence of 3×10^{13} $ions/cm^2$. Such significant change in the size of the crystallites at higher fluence may be due to annealing effect of SHI irradiation. In the case of high fluence ($> 1 \times 10^{12}$ $ions/cm^2$) material spends almost entire time during irradiation at equilibrium temperature of $\sim$ 834 K and feels annealing like atmosphere for whole irradiation period (see section-3.2). In contrast to the crystallite size of the as-deposited and irradiated thin films, the annealed films clearly indicate improved crystallinity with thermal treatment. From W-H plots, it is clear that the grain growth has occurred on thermal annealing at 850^{o}C.

Furthermore, we have calculated macro-strains of all the samples along a and c directions with the help of the following relations:-

$$\varepsilon_a^{'} = \frac{(a - a_o)}{a_o} \tag{10}$$

$$\varepsilon_c^{'} = \frac{(c - c_o)}{c_o} \tag{11}$$

Where a_o and c_o are the lattice parameters of the defect free sample ($a_o = 4.7433$ $\mathring{A}$ and $c_o = 3.1948$ $\mathring{A}$). The obtained values of $\varepsilon_a^{'}$ and $\varepsilon_c^{'}$ for all the samples are listed in Table 5 and plotted in Fig 10.

It is important to note that the Williamson-Hall method probes the micro-strain induced by dislocation inside the crystalline grains, i.e., opposite to a macro-strain that causes a shift in the Bragg peak position because of the presence of expansion/contraction type point defects [16]. We observed a decrease in the micro-strain and an increase in the macro-strain up to the fluence of 3×10^{13} $ions/cm^2$ (see Fig. 10). By inspection of the W-H plots, it appears that the micro-strain of pristine film is of the 10^{-3} order. The reduction of micro-strain after irradiation is indicative of the

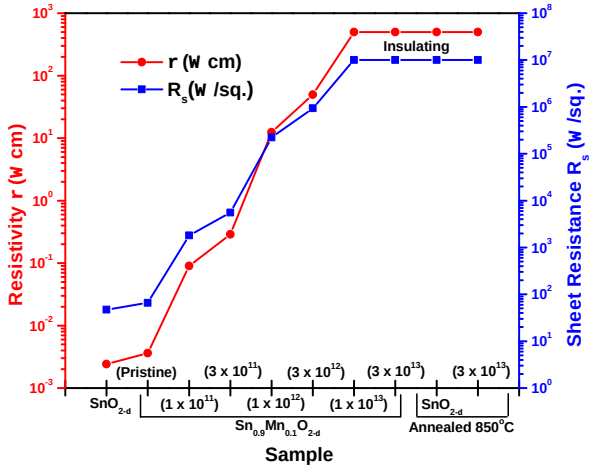

Figure 11: Changes in the electrical resistivity ρ and sheet resistance R_s of respective samples. Here x-axis is not scaled for better clarity.

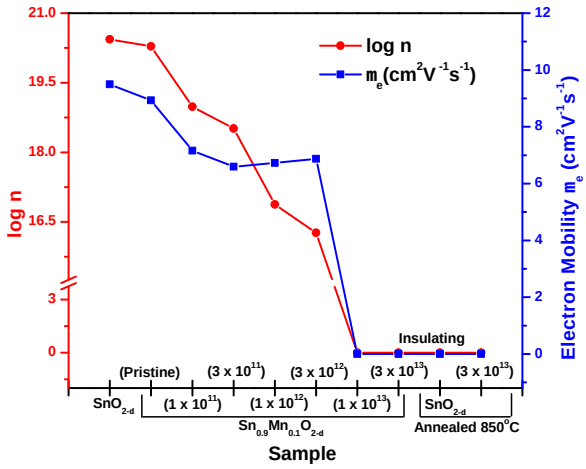

Figure 12: Changes in the free carrier concentration n and electron mobility μ_e of respective samples. Here x-axis is not scaled for better clarity.

improvement in crystallinity due to self-annealing of pre-existing irregular lattice defects such as dislocations, faults etc. Practically, it has been found that the higher the ion fluence, more is the heat generated, and hence smaller the micro-strain. The increase in macro-strain after SHI irradiation may be due to the formation of fresh regular expansion/contraction type point defects. It can be clearly seen from the Table 5, the macro-strain is of tensile type upto 3×10^{12} $ions/cm^2$ fluence and after that it is of compressive type. That is because before 1×10^{13} $ions/cm^2$ fluence the density of expansion type defects is more as compare to contraction type defects and it is vice versa for 1×10^{13} and 3×10^{13} $ions/cm^2$ fluence (already discussed in the XRD section). The micro-strain for the unirradiated pure SnO_2 sample is measured as 12.5×10^{-4}, which changes to 2.51×10^{-4} after annealing at 850^o (see Fig. 10). If we compare the micro-strain of pure SnO_2 samples annealed at 850^oC with samples irradiated at 3×10^{13} $ions/cm^2$ fluence, we find that high fluence irradiation more efficiently releases micro-strain from the samples. The macro-strain was also found to be negligibly small for the annealed samples (pure SnO_2 and irradiated at 3×10^{13} $ions/cm^2$ fluence). The reduction in micro- and macro-strain values after thermal annealing may be due to the migration of lattice defects at 850^oC.

3.6. Electrical properties

The electrical properties of the films were estimated by resistivity and Hall effect measurements made at room temperature. The room temperature results are presented for all measured films in Table 6. The pure SnO_2 film shows the best combination of electrical properties as follows: resistivity (ρ) of 2.41×10^{-3} Ω cm, carrier concentration (n) of 2.735×10^{20} cm^{-3}, and mobility (μ) of 9.497 $cm^2V^{-1}s^{-1}$. The electrical resistivity of 3.63×10^{-3} Ω cm obtained from the pristine $Sn_{0.9}Mn_{0.1}O_{2-\delta}$ films is increased to 49.6 Ω cm for the films irradiated with 3×10^{12} $ions/cm^2$ fluence (see Fig. 11). The value of carrier concentration for pristine sample is 1.927×10^{20} cm^{-3} and is reduced to 9.658×10^{18}, 3.283×10^{18}, 7.492×10^{16}, 1.831×10^{16} cm^{-3} for films irradiated with the fluence of 1×10^{11}, 3×10^{11}, 1×10^{12}, and 3×10^{12} $ions/cm^2$, respectively (see Fig. 12). On the other hand, the mobility of

Table 6: Electrical parameters for all the samples.

Samples	Film thickness t (nm)	Sheet resistance R_s	Resistivity ρ (Ω cm)	Carrier concentration n (cm^{-3})	Degeneracy temperature T_D (K)	Carrier mobility μ ($cm^2V^{-1}s^{-1}$)	
						Observed	Calculated
$SnO_{2-\delta}$	510	47 $\Omega/\square$	2.41×10^{-3}	2.735×10^{20}	5767	9.497	10.346
$Sn_{0.9}Mn_{0.1}O_{2-\delta}$ (Pristine)	550	66 $\Omega/\square$	3.63×10^{-3}	1.927×10^{20}	4566	8.929	-
1×10^{11} $ions/cm^2$	500	1.81 $K\Omega/\square$	9.03×10^{-2}	9.658×10^{18}	621	7.163	-
3×10^{11} $ions/cm^2$	523	5.53 $K\Omega/\square$	0.289	3.283×10^{18}	302	6.597	-
1×10^{12} $ions/cm^2$	555	0.223 $M\Omega/\square$	12.4	7.492×10^{16}	24	6.724	-
3×10^{12} $ions/cm^2$	530	0.936 $M\Omega/\square$	49.6	1.831×10^{16}	10	6.875	-
1×10^{13} $ions/cm^2$	515	$\approx$10 $M\Omega/\square$	-	-	-	-	-
3×10^{13} $ions/cm^2$	505	$\approx$10 $M\Omega/\square$	-	-	-	-	-
Annealed 850^oC ($SnO_{2-\delta}$)	510	$\approx$10 $M\Omega/\square$	-	-	-	-	-
Annealed 850^oC (3×10^{13} $ions/cm^2$)	505	$\approx$10 $M\Omega/\square$	-	-	-	-	-

$Sn_{0.9}Mn_{0.1}O_{2-\delta}$ films is decreased from the original value of 8.929 $cm^2V^{-1}s^{-1}$ to 6.875 $cm^2V^{-1}s^{-1}$ after irradiation with fluence of 3×10^{12} $ions/cm^2$ (see Fig. 12). Above a typical fluence of 3×10^{12} $ions/cm^2$, electrical measurements show that the sheet resistance of irradiated film is of the order of 10 M$\Omega/\square$ (see Fig. 11). In addition, thermally annealed films also reflect insulating resistance behaviour.

In this section, we will briefly discuss the role of native point defects and impurities on the n-type conductivity of SnO_2. This discussion will help us later to explain the electrical properties of the pristine and irradiated films. Point defects are usually electrically active and introduce levels in the band gap of semiconductor. These levels involve transitions between different charge states of the same defect. Transition levels can be derived directly from the calculated formation energies [159-161]. In semiconductor there may exist two types of transition levels: shallow and deep. This distinction is on the basis of their position in the energy band with respect to valence or conduction band. For a defect to contribute to n-type conductivity, it must be stable in a positive charge state and the transition level from the positive to neutral charge state $\epsilon(+/0)$ should occur close to or above the conduction band minimum (CBM). Shallow donors are defects in which the transition level from a positive to the neutral charge state $\epsilon(+/0)$ is near or above the CBM. Theoretical studies based on density functional theory have contributed to deeper understanding of the role of point defects on the unintentional n-type conductivity in SnO_2 [41-45, 82, 83, 92-98]. For a long time it has been envisaged that the unintentional n-type conductivity in SnO_2 is caused by the presence of oxygen vacancies (V_O) and tin interstitials (Sn_i) [44]. However, recent first principle calculations have demonstrated that this attribution to native point defects cannot be correct [41, 42]. It has been shown that oxygen vacancies are very deep rather than shallow donors and therefore cannot contribute to n-type conductivity. According

to Singh et. al. [42], the $\epsilon(2+/0)$ transitional level is located at 1.24 eV above the VBM in GGA and at 1.39 eV in GGA + U; the extrapolated value is 1.80 eV. This result distinctly shows that V_O^0 is a deep donor with ionization energy of 1.8 eV. In addition, it was found that tin interstitials (Sn_i^{4+}) and tin antisites (Sn_O^{4+}) are also unlikely causes of the unintentional n-type conductivity in as-deposited SnO_2 films [42]. The tin interstitial is a shallow donor, but it is not thermally stable. It has high formation energy about 12 eV in n-type SnO_2 and migrates through the interstitial channels along the [001] direction with an energy barrier of only 0.13 eV. This very low energy barrier implies that the Sn interstitials are highly mobile even below room temperature. Tin antisites are also shallow donors but their high formation energies make them unlikely to exist in measurable concentrations under equilibrium conditions. The dissociation barrier of Sn_O^{4+} into Sn_i^{4+} and V_O^0 is very high in n-type SnO_2. Therefore, Sn_O^{4+} is expected to be stable at temperature of up to 500 K. This suggest that Sn_O^{4+} may play a role in n-type conductivity under non-equilibrium conditions such as ion beam irradiation. On the other hand Sn vacancies (V_{Sn}^{4-}) are deep acceptors and have lowest formation energies among the native point defects under n-type conditions [42, 82, 92, 93]. They can therefore occur as a compensating defects in n-type SnO_2. In contrast, oxygen antisites (O_{Sn}^{2-}) have the highest formation energies among the acceptor type native defects [82, 92, 93]. Hence, it is very unlikely that oxygen antisites would be present in equilibrium. However, O_{Sn}^{2-} could potentially be created under non-equilibrium conditions in n-type SnO_2. Oxygen antisites are also deep acceptors and show large off site displacements, in which the oxygen atom forms a chemical bond with one of the oxygen nearest neighbours. Oxygen interstitials (O_i) can exist either as electrically inactive split interstitials in p-type samples or as a deep acceptors at the octahedral sites in n-type samples [82, 92, 93]. In both forms oxygen interstitials have high formation energies and are therefore unlikely to be present in measurable concentrations under equilibrium conditions. A key conclusion from the recent DFT studies [41, 42, 82, 92, 93, 97, 98] is that native point defects cannot explain the unintentional n-type conductivity. One has to consider the role of impurities that are most likely to be present in different growth and processing environments and act as shallow donors. Hydrogen is indeed a especially ambidextrous impurity in this respect, since it is extremely difficult to detect experimentally [82, 93]. By means of density-functional calculations it has been shown that interstitial hydrogen (H_i^+) forms a strong bond with an oxygen atom with an O-H bond length of 1.04 $\dot{A}$ in SnO_2 and act as a shallow donor [42]. However, interstitial hydrogen is highly mobile and can easily diffuse out of the SnO_2 samples. Its migration path involves breaking and forming of O-H bonds with a nearest neighbour oxygen atom. The migration barrier of interstitial hydrogen is only 0.57 eV [42]. This low barrier value makes it difficult to explain the stability of the n-type conductivity at relatively high temperature. More recently, it has been suggested that hydrogen can also substitute on an oxygen site in SnO_2 and act as shallow donor [42]. Substitutional hydrogen (H_0^+) is much more thermally stable than interstitial hydrogen (H_i^+) and can explain stability of n-type conductivity at high temperature and its variation with partial pressure of oxygen [162-165]. Both the substitutional and interstitial forms of hydrogen have low formation energies in SnO_2, indicating that they can occur in significant concentrations. Table 3 lists the details of all native point defects and hydrogen impurities.

From above discussion we can conclude that substitutional hydrogen (H_0^+) and tin antisite (Sn_O^{4+}) are liable as a source of n-type conductivity in pristine and irradiated samples, respectively. In addition to tin antisite, some acceptor type point defects such as V_{Sn}^{4-}, O_i^{2-} and O_{Sn}^{2-} may also be present in irradiated samples, which try to eliminate existing n-type conductivity. In n-type SnO_2, tin vacancies have the lowest formation energy among the native point defects. Therefore they may exist as compensating defects also in n-type pristine sample. But if we make thin films at a specific temperature somewhere in between migration temperature of tin vacancy and substitutional hydrogen, we find that they are highly conducting ($n \geq 10^{20}\ cm^{-3}$).

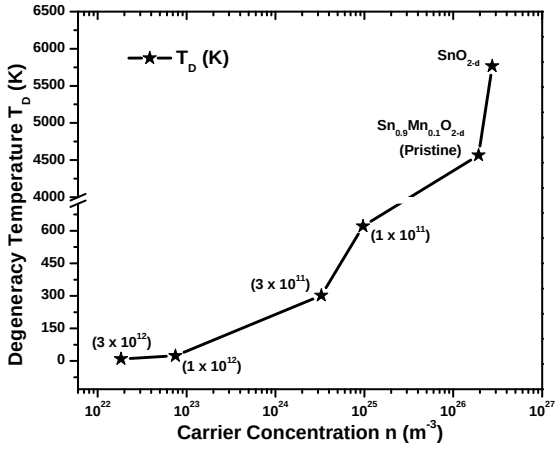

Figure 13: Degeneracy temperature as a function of carrier concentration.

In the present investigation, we have optimised substrate temperature for the deposition of SnO_2 thin films at 450^o C. This substrate temperature is much higher than the migration temperature of tin vacancy. Thus we can say that the n-type conductivity in pristine samples may be caused by H_O^+ defects. SHI irradiation is very effective method to keep the sample at very high temperature through electron-phonon coupling in a short span of time. Due to this self annealing effect of irradiation, the concentration of pre-existing defects (H_O^+) decreases with increasing ion fluence. Along with this self annealing of pre-existing defects, some fresh electron donor (Sn_O^{4+}) and electron killer (V_{Sn}^{4-}, O_i^{2-}, O_{Sn}^{2-}) type defects can be formed through irradiation in the target. The variation in conductivity of irradiated samples may be caused by these mixed effects. The point defects newly created by ion beam irradiation can also be annealed out of the sample at high fluence ($\geq 1 \times 10^{13}$ $ions/cm^2$). In the case of high fluence, target sample spends almost entire time during irradiation at equilibrium temperature ($\sim$ 834 K). Therefore in that case all those newly created defects may anneal out of the sample whose migration temperature is less than the equilibrium temperature. Among the all possible defects only V_O^0 defect has a higher migration temperature ($\sim$ 900 K) than the equilibrium temperature ($\sim$ 834 K). That's why all the other newly created defects ($V_{Sn}^{4-}, O_i^{2-}, Sn_O^{4+}, O_{Sn}^{2-}$) except V_O^0 defect may anneal out of the sample during high fluence irradiation. With the help of these arguments one can understand the insulating behaviour of high fluence irradiated samples. Thermal annealing of conducting SnO_2 films was also carried out beyond the migration temperature of H_O^+ defects ($\sim$ 900 K) to confirm the role of H_O^+ defects on the film resistivity.

The temperature dependence of electrical resistivity in the range 30-200^oC indicates that the pure and Mn doped SnO_2 (pristine) films are degenerate semiconductors. The film degeneracy was further confirmed by evaluating degeneracy temperature of the electron gas T_D by the expression [166, 167]:

$$k_B T_D \simeq (\frac{\hbar^2}{2m^*})(3\pi^2 n)^{\frac{2}{3}} = E_F, \qquad (12)$$

where m^* is the reduce effective mass and n is the electron concentration. The degeneracy temperature of all investigated samples is clearly displayed in Fig. 13. It can be seen that T_D of SnO_2 and $Sn_{0.9}Mn_{0.1}O_{2-\delta}$ (pristine) films are well above room temperature, both at around 5000 K.

In this section, we have tried to identify the main scattering mechanisms that influence the mobility of pure SnO_2 films. There are many scattering mechanisms such as grain-boundary scattering, domain scattering, surface scattering, interface scattering, phonon scattering (lattice vibration), neutral, and ionized impurity scattering which may influence the mobility of the films [168, 169]. The interaction between the scattering centres and the carriers determines the actual value of the mobility of the carriers in the samples. In the interpretation of the mobility obtained for pure SnO_2 films, one has to deal with the problem of mixed scattering of carriers. To solve this problem, one has to identify the main scattering mechanism and then determine their contributions. The pure SnO_2 films prepared here are polycrystalline. They

are composed of grains joined together by grain boundaries, which are transitional regions between different orientations of neighboring grains. These boundaries between grains play a significant role in the scattering of charge carriers in polycrystalline thin films. The grain boundary scattering has an effect on the total mobility only if the grain size is approximately of the same order as the mean free path of the charge carriers ($D \sim \lambda$). The mean free path for the degenerate samples can be calculated from known mobility (μ) and carrier concentration (n) using the following expression [167, 169]:

$$\lambda = (3\pi^2)^{\frac{1}{3}}(\frac{\hbar\mu}{e})n^{\frac{1}{3}}, \tag{13}$$

The mean free path value calculated for the pure SnO_2 film is 1.616 nm which is considerable shorter than crystallite size (D $\sim$ 30 nm) calculated using XRD data. Moreover, the effect of crystallite interfaces is weaker in semiconductors, with n $\geq$ 10^{20} cm^{-3}, observed here, as a consequence of the narrower depletion layer width at the interface between two grains [170]. Based on above discussion it is concluded that grain boundary scattering is not a dominant mechanism.

The mobility of the free carrier is not affected by surface scattering unless the mean free path is comparable to the film thickness [171]. Mean free path value calculated for the pure SnO_2 film is 1.616 nm, which is much smaller than the film thickness (t$\sim$510 nm). Hence, surface scattering can be ruled out as the primary mechanism. Scattering by acoustical phonons [172] apparently plays a subordinate role in the pure SnO_2 films because no remarkable temperature dependence have been observed between 30 and 200^{o}C. Moreover, neutral impurity scattering can be neglected because the neutral defect concentration is negligible in the pure SnO_2 films [167, 169]. Electron-electron scattering, as suggested to be important in Ref. 169, can also be neglected as it does not change the total electron momentum and thus not the mobility. In high crystalline SnO_2 films, scattering by dislocations and precipitation is expected to be of little importance [173].

Another scattering mechanism popular in unintentionally doped semiconductors is the ionized impurity scattering. According to the Brooks-Herring formula [174], the relaxation time for coupling to ionized impurities is in the degenerate case, given by

$$\tau_i = \frac{(2m^*)^{\frac{1}{2}}(\epsilon_o\epsilon_r)^2(E_F)^{\frac{3}{2}}}{\pi e^4 N_i f(x)}, \tag{14}$$

with N_i the carrier concentration of ionized impurities and f(x) given by

$$f(x) = ln(1+x) - \frac{x}{1+x}, \tag{15}$$

with

$$x = \frac{8m^* E_F R_S^2}{\hbar^2}, \tag{16}$$

The screening radius R_S is given by

$$R_S = (\frac{\hbar}{2e})(\frac{\epsilon_o\epsilon_r}{m^*})^{\frac{1}{2}}(\frac{\pi}{3N_i})^{\frac{1}{6}}, \tag{17}$$

where ϵ_r is the relative dielectric permittivity and m^* is the effective mass of the carriers. The mobility (μ) is defined as

$$\mu = \frac{e\tau}{m^*}, \tag{18}$$

Substitution of the τ_i expression [Eq. (14)] in Eq. (18) yields the expression for mobility due to ionized impurities as

$$\mu_i = \frac{(\frac{2}{m^*})^{\frac{1}{2}}(\epsilon_o\epsilon_r)^2(E_F)^{\frac{3}{2}}}{\pi e^4 N_i f(x)}, \tag{19}$$

Since all the H_O^+ defects present in the pure SnO_2 films will be fully ionized at room temperature, impurity ion concentration will be equal to the free carrier concentration. Thus taking N_i = n, $m^* = 0.31$m, $\epsilon_r = 13.5$ [74] and using Eq. (12) in Eq. (19) we get simplified form as

$$\mu_i = \frac{2.4232 \times 10^{-4}}{f(x)}, \tag{20}$$

with

$$x = 1.7942 \times 10^{-9} n^{\frac{1}{3}}, \tag{21}$$

The calculated mobility and measured mobility values for pure SnO_2 thin films are 10.346 and

9.497 $cm^2V^{-1}s^{-1}$ respectively, both are comparable to each other. This clearly indicates that the main scattering mechanism reducing the intra-grain mobility of the electrons in pure SnO_2 films is the ionized impurity scattering. Ionized impurity scattering with singly ionized H_O^+ donors best describes the mobility of pure SnO_2 samples. This finding supports our assumption that H_O^+ defect is source of conductivity in pure SnO_2 sample.

A Coulomb interactions between the electrons and the ionized impurities cause collisions and the scattering of the electrons. The amount of deflection depends on the speed of the electron and its proximity to the ion. The electrons will not experience the Coulombic force if they do not spend much time near the ionized impurities. If the electrons are moving fast, the amount of time spent in the location of the ionized impurity will be very short. This will affect the mobility of the electrons. Temperature of the material greatly affects ionized impurity scattering. At low temperatures, the electrons are moving slowly because thermal velocity is low. If the thermal velocity of the electrons is small, the amount of time the electrons stay within the vicinity of an ionized impurity increases. This increases the cross section of scattering. Another factor affecting ionized impurity scattering is the concentration of ionized impurities. The more ionized impurities in the material; the more scattering events occur. With the higher probability of scattering event, the mean time between collisions decrease, which decreases mobility. The mobility of electrons in non-degenerate semiconductor increases with temperature and is independent of the electron concentration, whereas the mobility in a highly degenerate semiconductor is nearly independent of temperature and increases with electron concentration [175, 176].

3.7. Microstructural properties

Structural characterization through TEM is a direct way of visualizing the estimated grain size. It also gives authentic information regarding the grain size distribution, crystalline nature, and other structural information. The transmission electron micrographs and the corresponding selected area electron diffraction (SAED) patterns for $SnO_{2-\delta}$ and $Sn_{0.9}Mn_{0.1}O_{2-\delta}$ samples are shown in Fig. 14. These TEM micrographs and SAED patterns have been analyzed using the IMAGE-J software. The TEM images of the $SnO_{2-\delta}$ and $Sn_{0.9}Mn_{0.1}O_{2-\delta}$ samples show the presence of interconnected nonosized spheroidal grains. The crystallite size observed by TEM ($\sim$ 25 nm for $SnO_{2-\delta}$ and $\sim$ 30 nm for $Sn_{0.9}Mn_{0.1}O_{2-\delta}$) is in good agreement with that estimated by x-ray line broadening ($\sim$ 27 nm for $SnO_{2-\delta}$ and $\sim$ 29 nm for $Sn_{0.9}Mn_{0.1}O_{2-\delta}$). The SAED patterns shown in Figs. 14(b) & 14(d) taken from $SnO_{2-\delta}$ and $Sn_{0.9}Mn_{0.1}O_{2-\delta}$ samples show several sharp rings, which are indexed to the (110), (101), (211) and (301) planes of the rutile crystalline structure of SnO_2. The SAED pattern has been examined carefully for spots/rings of secondary phases, and it has been found that all the spots/rings belong to the SnO_2 rutile phase only. We have observed that there is no formation of any structural core-shell system.

The SEM images of $SnO_{2-\delta}$ and $Sn_{0.9}Mn_{0.1}O_{2-\delta}$ thin films deposited by chemical spray pyrolysis technique at substrate temperature of 450^oC are shown in Fig. 15. The SEM images reveal significant aggregation of the nano-grains. The small grains coagulated to form big clusters that reflect like the pomegranate structure [177]. This agglomeration is because of the fact that smaller primary grains have a large surface free energy and would, therefore, tend to agglomerate faster and grow into larger particles/clusters. The aggregation of nano-grains is very important for the ferromagnetism in nano-crystalline oxides [178], which can increase the domain size and generate lattice defects. In our samples, the aggregation should be promising for ferromagnetism. The aggregation makes it difficult to determinate the grain size accurately. The size that is estimated from the few spherical grains is about 25 nm. This is slightly smaller than that obtained from XRD measurements.

AFM images (Figs. 16(a) and 16(b)) of samples irradiated at 3×10^{12} and 3×10^{13} $ions/cm^2$ fluence show a blister-like surface topology with

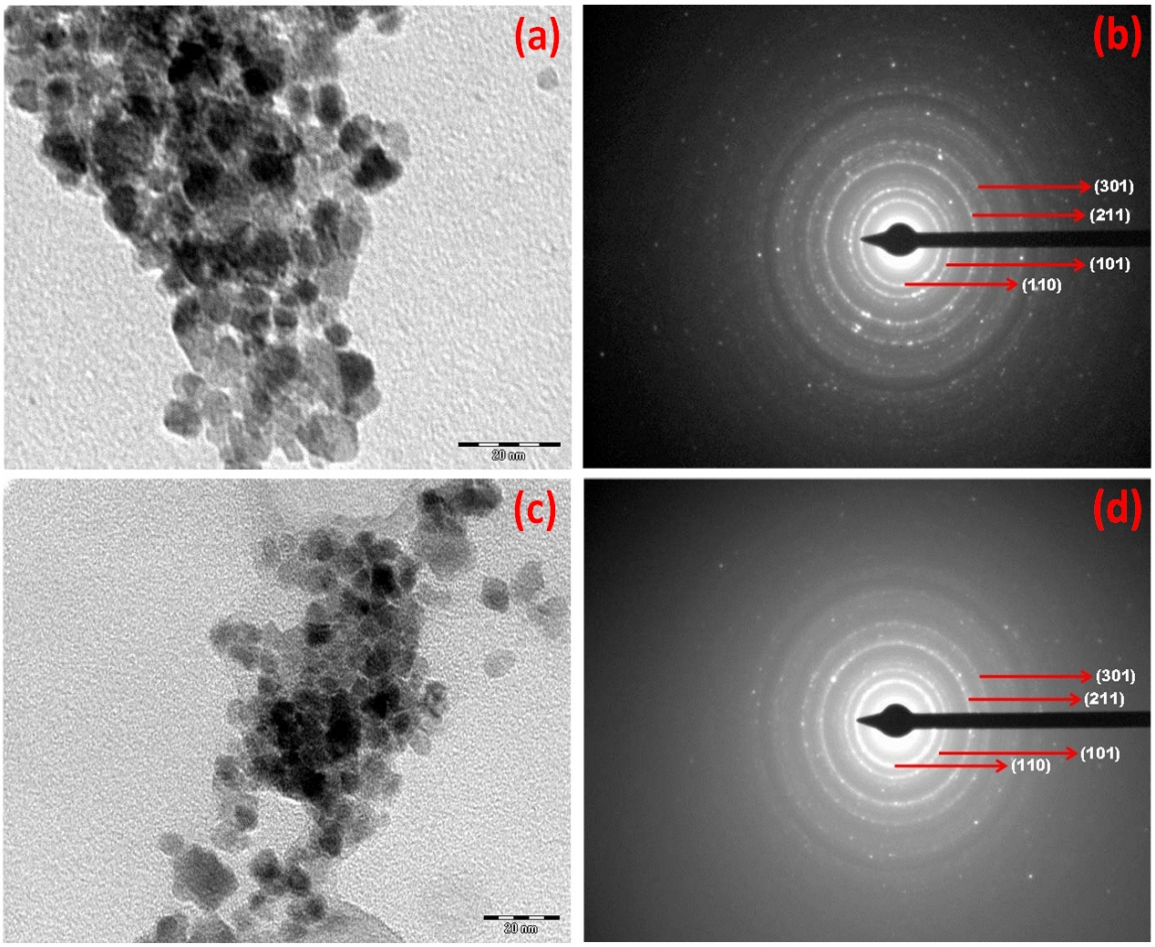

Figure 14: Transmission electron micrographs [(a) and (c)] of the pure $SnO_{2-\delta}$ and pristine $Sn_{0.9}Mn_{0.1}O_{2-\delta}$ thin films, respectively. Corresponding selected area electron diffraction (SAED) patterns for the pure $SnO_{2-\delta}$ and pristine $Sn_{0.9}Mn_{0.1}O_{2-\delta}$ thin films are shown in (b) and (d), respectively. Transmission electron micrographs of both thin films showing several nanocubes or nanospheres.

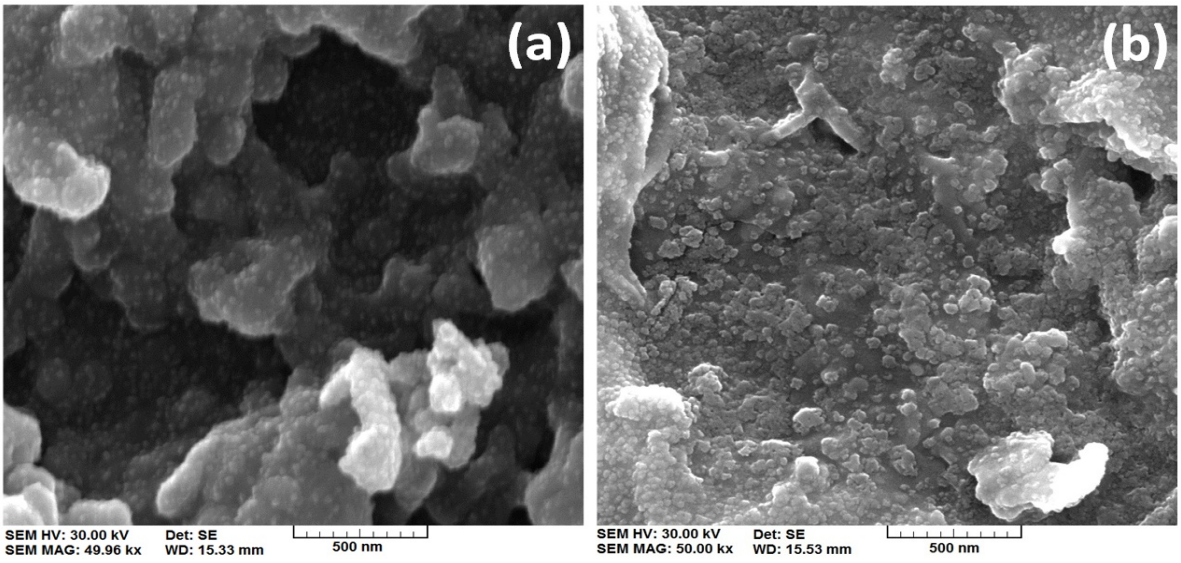

Figure 15: Scanning electron micrographs of the (a) pure $SnO_{2-\delta}$ and (b) pristine $Sn_{0.9}Mn_{0.1}O_{2-\delta}$ thin films.

rms roughness of 10.3 and 5.6 nm, respectively. In addition to roughness variation, AFM images also show an increase in grain size with increasing ion fluence from 3×10^{12} to 3×10^{13} $ions/cm^2$. From the XRD analysis, it is clear that the grain/crystallite size of irradiated samples remains nearly the same upto fluence of 1×10^{12} $ions/cm^2$, whereas for high fluence it increases significantly. That is because in the case of high fluence ($> 1 \times 10^{12}$ $ions/cm^2$) target material spends almost entire time during irradiation at equilibrium temperature of T $\sim$ 834K (see Section 3.2) and feels annealing like atmosphere for whole irradiation period, which is quite long about 2 hrs 40 mins for 3×10^{13} $ions/cm^2$ fluence. Fig. 16(c) shows the morphology of $Sn_{0.9}Mn_{0.1}O_{2-\delta}$ sample irradiated with 3×10^{13} $ions/cm^2$ fluence and then annealed at 850^oC for 4hrs. After annealing, the grains of irradiated films become nearly spherical in shape with size in the range of 100 to 150 nm and rms roughness of 16.5 nm. The increment in grain size is caused due to the thermal heating induced growth in crystallinity. Fig. 16(d) shows the surface of the film annealed at 850^oC and then irradiated with 3×10^{13} $ions/cm^2$ fluence. Morphology of this film is very much different from that shown in Fig. 16(c). At this condition nanorod like structures with size in the range of 50-100 nm and rms roughness of 6.4 nm are formed in a particular direction. Morphological changes in the film after irradiation depend on the conductivity of target material. If the target material is a conductor ($n \geq 10^{20} cm^{-3}$ for as-deposited $Sn_{0.9}Mn_{0.1}O_{2-\delta}$ film) then conduction electrons rapidly spread the energy of incident ion throughout the material and we find similar pristine/target sample like morphology with some dimensional change after irradiation (see Figs. 16(a), 16(b) & 16(c)). But if target material is insulator (such as $Sn_{0.9}Mn_{0.1}O_{2-\delta}$ sample annealed at 850^oC) then projectile ions can not spread their energy throughout the target material and therefore they create high energy region in the close vicinity of their paths. This cylindrical region around the path of the ion may become fluid if maximum temperature reached at the centre is higher than the

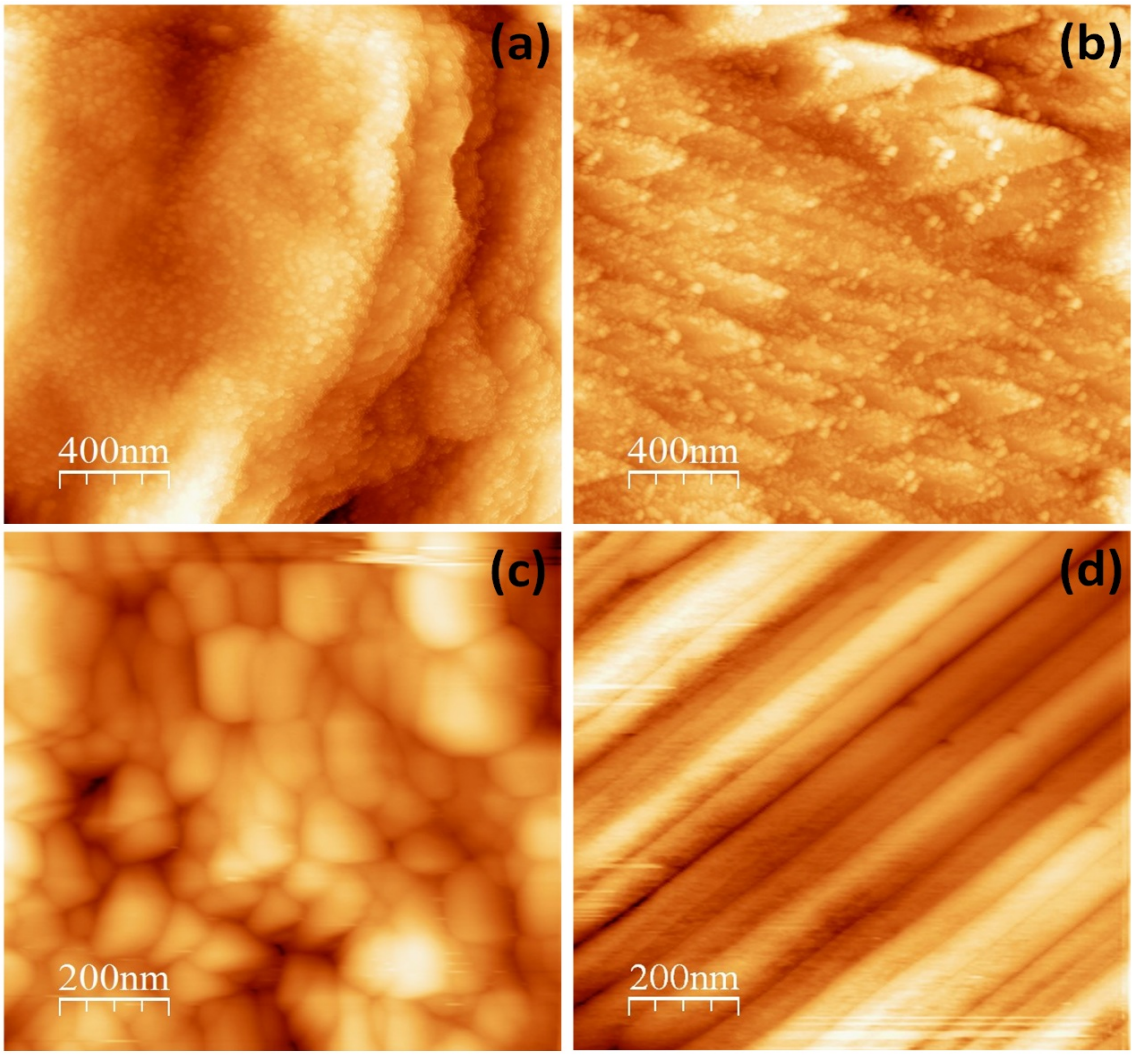

Figure 16: (a) Atomic force microscopy images of $Sn_{0.9}Mn_{0.1}O_{2-\delta}$ surfaces: (a) irradiated with 3×10^{12} ions/cm^2, (b) irradiated with 3×10^{13} ions/cm^2, (c) annealed at 850^oC after irradiation with 3×10^{13} ions/cm^2, (d) irradiated with 3×10^{13} ions/cm^2 after annealing at 850^oC.

melting temperature of the material. The structure of grains is changed (spherical to rod like) only when melting is observed and the nature/size of the new structure corresponded closely to the maximum molten region. In the present case, amorphous nanorods like structures (see Fig. 16(d)) may arise from overlapping and reconstruction of melted material. Further effort is under progress to explain role of carrier concentration in such morphological changes.

3.8. Band-gap and Transmittance studies

The effect of defects (donors or acceptors) on the energy gap of semiconductors has both scientific and engineering, theoretical and practical importance. For the physicist, it is a manifestation of subtle effects that are difficult to detect and measure. For applied scientist, the energy gap is an essential parameter needed to design devices and to predict their performance. The presumed band structure of SnO_2 is shown in Fig. 17 with the parabolic conduction and valence bands. With the top of the valence band as reference energy, the dispersion relations for the unperturbed valence and conduction bands are

$$E_v^0(k) = \frac{-\hbar^2 k^2}{2m_v^*}, \tag{22}$$

and

$$E_c^0(k) = E_{g0} + \frac{\hbar^2 k^2}{2m_c^*}, \tag{23}$$

respectively. E_{g0} is the intrinsic band gap of the semiconductor, k = $\frac{2\pi}{\lambda}$ is the wave number, and superscript 0 denotes unperturbed bands. When the carrier density n exceeds the Mott critical density [179], $n_c^{1/3} a_0^* \sim 0.25$ (a_0^* is the effective Bohr radius), the low-energy levels of conduction band are filled up by the conduction electrons [180, 181]. Then photons with energy greater than the intrinsic band gap only get absorbed. Hence, the energy gap for direct transitions in the degenerate semiconductor is then given in terms of the unperturbed bands as

$$E_g = E_c^0(k_F) - E_v^0(k_F), \tag{24}$$

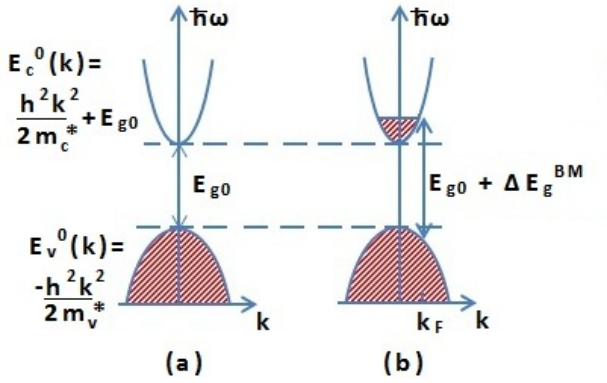

Figure 17: (a) Schematic band structure of stoichiometric SnO_2 showing the parabolic conduction and valence bands separated by the band gap E_{g0} and (b) the Burstein-Moss shift ΔE_g^{BM} due to filling up of the lowest states in the conduction band. Shaded areas denote occupied regions. Band gaps, Fermi wave number, and dispersion relations are indicated.

where $k_F = (3\pi^2 n_e)^{\frac{1}{3}}$ is the Fermi wave number. Alternatively, we may write

$$E_g = E_{g0} + \Delta E_g^{BM}, \tag{25}$$

where the Burstein-Moss (BM) shift [180, 181] is given by

$$\Delta E_g^{BM} = [E_c^0(k_F) - E_v^0(k_F)] - E_{g0},$$

$$\Delta E_g^{BM} = \frac{\hbar^2}{2m_{vc}^*}(3\pi^2 n_e)^{2/3}, \tag{26}$$

with the reduced effective mass

$$\frac{1}{m_{vc}^*} = \frac{1}{m_v^*} + \frac{1}{m_c^*}, \tag{27}$$

Neglecting the electron-electron and electron-defect interactions [182, 183], the band gap is

$$E_g = E_{g0} + \frac{\hbar^2}{2m_{vc}^*}(3\pi^2 n_e)^{2/3} \tag{28}$$

The optical band gap E_g of films may be determined from the spectral dependence of the absorption coefficient α by the application of existing theories. It

is known that the absorption coefficient α depends on the type of transition of carriers from valence to conduction band due to incident photons. Now, α may be written in terms of optical band gap E_g and incident photon energy $h\nu$ as follows [184]:

$$\alpha = \frac{[A(h\nu - E_g)^n]}{h\nu} \tag{29}$$

where A is a constant which is different for different transitions indicated by different values of superscript n, and E_g is the corresponding band gap. For direct transitions n = 1/2 or n = 2/3, while for indirect ones n = 2 or 3, depending on whether they are allowed or forbidden, respectively [184]. The band gap can be deduced from a plot of $(\alpha h\nu)^2$ versus photon energy $(h\nu)$. Better linearity of these plots suggests that the films have direct band transition. The extrapolation of the linear portion of the $(\alpha h\nu)^2$ vs. $h\nu$ plot to $\alpha = 0$ will give the band gap value of the films [185]. Fig. 18 shows such plots for all the samples and the linear fits obtained for these plots are also depicted in the same figure.

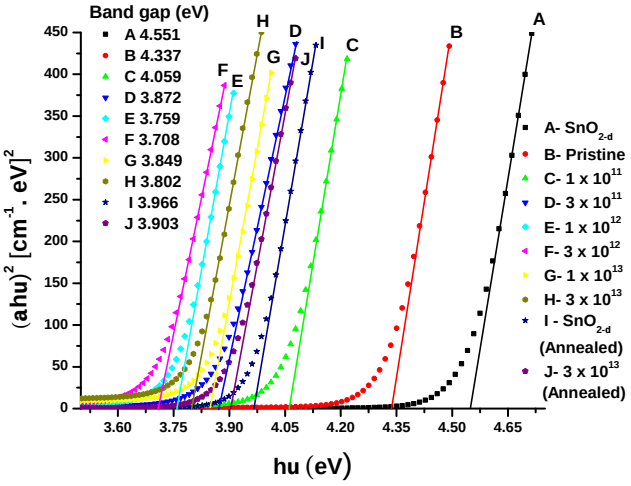

Figure 18: $(\alpha h\nu)^2$ vs $h\nu$ plots for the un-irradiated, irradiated and annealed samples. The direct energy band gap E_g is obtained from the extrapolation to $\alpha = 0$.

The Burstein-Moss effect [180, 181], i.e., the widening of the band gap with increasing n, is exhibited when the electron density (n) far exceeds the Mott critical density (n_c), whose magnitude can be estimated by Mott's criterion [179].

$$n_c^{1/3} a_0^* \sim 0.25 \tag{30}$$

The effective Bohr radius a_0^* is given by:

$$a_0^* = \frac{h^2 \epsilon_0 \epsilon_r}{\pi e^2 m_c^*} \tag{31}$$

where ϵ_r is the static dielectric constant of the host lattice (equals 13.5 for SnO_2 [74, 183]), and m_c^* is the effective mass of the electrons in the conduction band. After comparing experimental data of several authors, Sanon et. al. [183] calculated the effective mass of SnO_2 to be about one third of the electron rest mass; i.e. $m_c^* = 0.31$m. Using these numbers, one can obtain $a_0^* \sim 2.31$ nm, and the critical density n_c is calculated as $1.3 \times 10^{18}\ cm^{-3}$. Above this Mott critical density, the material is said to be degenerate.

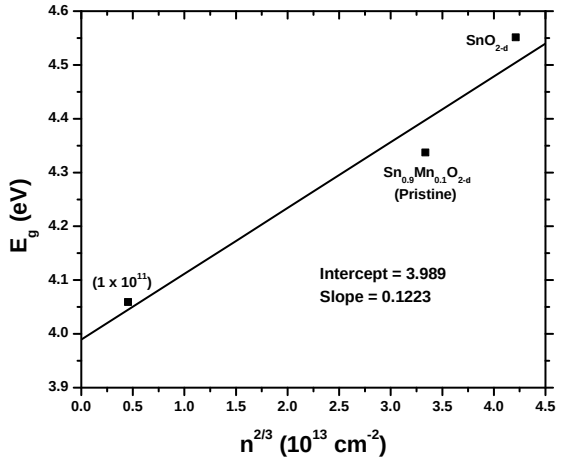

Figure 19: Band gap as a function of carrier concentration for the degenerate samples ($SnO_{2-\delta}$, $Sn_{0.9}Mn_{0.1}O_{2-\delta}$ and SHI: 1×10^{11} $ions/cm^2$). The linear-fit of the experimental data gives $E_{g0} = 3.99$ eV and $m_{vc}^* = 0.298$m.

For degenerate semiconductor (such as pure $SnO_{2-\delta}$, $Sn_{0.9}Mn_{0.1}O_{2-\delta}$ and 1×10^{11} $ions/cm^2$), a plot of E_g versus $n^{2/3}$ gives E_{g0} as well as m^*_{vc}. Such a plot is given in Fig. 19. From this plot, the intrinsic band gap E_{g0} and reduced effective mass m^*_{vc} come out to be 3.99 eV and 0.298m, respectively. As the valence-band effective mass is given by

$$m^*_v = \frac{m^*_c . m^*_{vc}}{m^*_c - m^*_{vc}} \tag{32}$$

Taking the conduction-band effective mass as m^*_c = 0.31m, m^*_v works out to be 7.69m for the present study. The high value of valence-band effective mass comes due to neglectance of electron-electron and electron-defect interactions. But, it can be noted that the reduced effective mass of SnO_2 obtained in the present work (m^*_{vc} = 0.298m) is comparable than that estimated for SnO_2 by Sanon et. al. [183] (m^*_{vc} = 0.237m) using m^*_c = 0.31m and m^*_v = 1.0m. The band-gap narrowing due to electron-electron and electron-defect scattering in SnO_2 films is quite significant and cannot be neglected. The narrowing when added to experimental widening yields the actual Burstein-Moss widening. Thus by including the many-body interactions in the valence-band and conduction bands, a positive small value of valence-band effective mass (m^*_v = 1.0m) may be obtained.

The band gap obtained for annealed SnO_2 sample can be assumed as exact intrinsic band gap. As we know, the migration energies of almost all point defects are less than 700^{o}C [41, 42, 43, 45, 82, 92, 93]. Therefore samples which have been annealed at a temperature of 850^{o}C, they may be free of defects. On comparing the band gap of annealed SnO_2 sample ($\sim$ 3.97 eV) with that estimated from Fig. 19 ($\sim$ 3.99 eV), we find that both are nearly same. For degenerate samples such as $SnO_{2-\delta}$, $Sn_{0.9}Mn_{0.1}O_{2-\delta}$ and 1×10^{11} $ions/cm^2$, it can be seen that the band gap is changing according to Burstein-Moss effect whereas for other irradiated samples (SHI: 3×10^{11} to 3×10^{13} $ions/cm^2$) we can notice a significant but small shift in band gap from intrinsic band gap (E_{g0} = 3.97 eV). This noticeable shift in the band gap upon irradiation (SHI: 3×10^{11} to 3×10^{13} $ions/cm^2$) may be due to creation of intermediate energy levels [186-189].

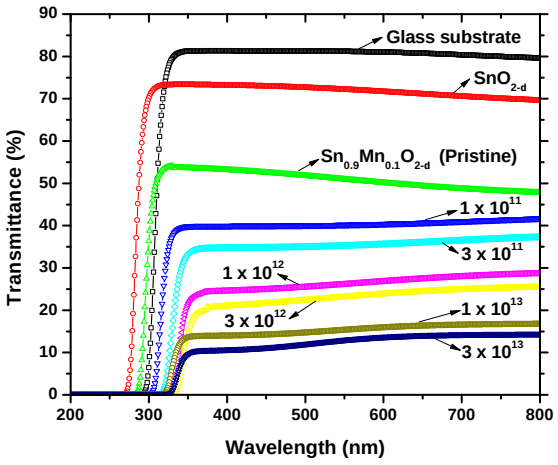

Figure 20: Comparison of transmittance spectra obtained from the different samples.

The optical transmittance spectra for un-irradiated (SnO_2 and $Sn_{0.9}Mn_{0.1}O_{2-\delta}$) and irradiated (SHI: 1×10^{11} - 3×10^{13} $ions/cm^2$) thin films are shown in Fig. 20. In the visible region, the average transmittance for the pure SnO_2 film is of $\sim$ 72%, which is decreased upto $\sim$ 50% on addition of 10 at.% of Mn. This relatively large absorption in $Sn_{0.9}Mn_{0.1}O_{2-\delta}$ film may be the result of mixed valence of Mn (Mn^{4+}/Mn^{3+}). It was reported by Kojima et. al. [190] that when a material contains an element in two different oxidation states or in a mixed oxidation state, it manifests abnormally deep and intense coloration. The reason is that electron transfer between the different oxidation states of the element causes intense light absorption. Moreover, the $Sn_{0.9}Mn_{0.1}O_{2-\delta}$ film exhibits a systematic decrease in the transmittance with increasing irradiation (SHI: 1×10^{11} - 3×10^{13} $ions/cm^2$) fluence. For the highest fluence, the transmittance of the $Sn_{0.9}Mn_{0.1}O_{2-\delta}$ film is substantially reduced to about 13%. The reduction in the optical trans-

mittance due to irradiation may result from the incorporation of V_O^0 lattice defects having absorption in the optical region. It is know that the transmittance of a transparent conducting film depends on the concentration of oxygen vacancy V_O^0 in the film [191, 192]. Films with greater concentration of oxygen vacancy V_O^0 will be less transparent. In our case, the concentration of V_O^0 defect increases with increasing irradiation fluence (SHI: 1×10^{11} - 3×10^{13} $ions/cm^2$). That's why transmittance of film decreases accordingly. Furthermore, the sharp decrease in transmittance at the shorter wavelength is as a result of the inter-band transition. In the present work, we have not observed fringes in the transmittance spectra. Normally, fringes appear in the transmittance spectra due to the interference of the light, reflected between air-film and film-substrate interfaces [193]. But, if the thickness is not uniform or slightly tapered then interference fringes may disappear from the transmission curve.

3.9. Magnetic properties

For proper investigation and understanding of the magnetic properties of pristine and irradiated $Sn_{0.9}Mn_{0.1}O_{2-\delta}$ films, measurements of magnetization as a function of temperature [M(T)] and magnetic field [M(H)] have been carried out over a temperature range of 5-300 K and field range of 0 to $\pm$ 2 T using a SQUID magnetometer. Figs. 21 and 22 show the magnetization versus applied magnetic field (M-H) curves measured at 5 and 300 K for the pristine and irradiated (SHI: 1×10^{11} and 3×10^{11} $ions/cm^2$) $Sn_{0.9}Mn_{0.1}O_{2-\delta}$ films with n = 1.9×10^{20}, 9.7×10^{18} and 3.3×10^{18} electrons cm^{-3} respectively. The magnetic field was applied parallel to the film plane. The inset of Figs. 21 and 22 shows a zoom of the region of low magnetic fields that evidences the presence of a hysteresis. The saturation magnetization (M_S) is estimated to be 14.503×10^{-2}, 10.013×10^{-2} and 3.745×10^{-2} emu/g at 5 K and 13.793×10^{-2}, 8.265×10^{-2} and 1.843×10^{-2} emu/g at 300 K and the coercivity (H_C) is 89, 45 and 29 Oe at 5 K and 83, 35 and 24 Oe at 300 K for the pristine and irradiated (SHI: 1×10^{11} and 3×10^{11} $ions/cm^2$) $Sn_{0.9}Mn_{0.1}O_{2-\delta}$ samples by the M-H curves, respectively. The

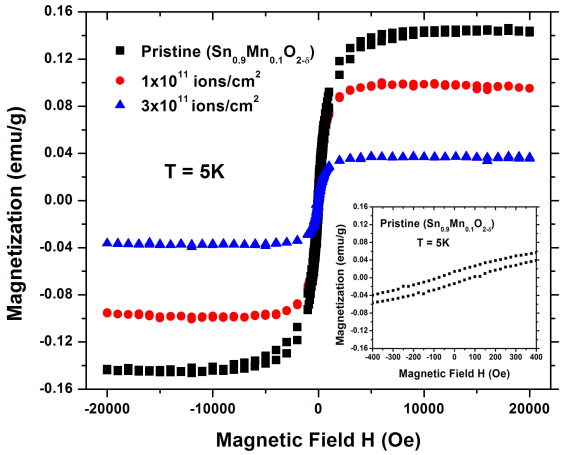

Figure 21: Field-dependent magnetization of the pristine and irradiated (SHI: 1×10^{11} and 3×10^{11} $ions/cm^2$) $Sn_{0.9}Mn_{0.1}O_{2-\delta}$ thin films measured at 5K. The inset shows the low-field part in an enlarged scale that evidences the presence of a hysteresis in pristine $Sn_{0.9}Mn_{0.1}O_{2-\delta}$ sample.

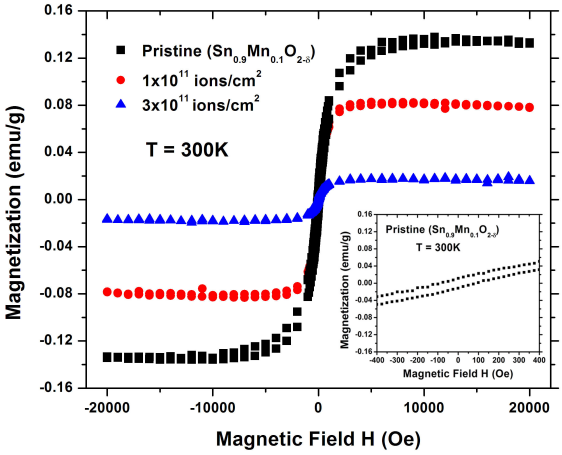

Figure 22: Field-dependent magnetization of the pristine and irradiated (SHI: 1×10^{11} and 3×10^{11} $ions/cm^2$) $Sn_{0.9}Mn_{0.1}O_{2-\delta}$ thin films measured at 300K. The inset shows the low-field part in an enlarged scale that evidences the presence of a hysteresis in pristine $Sn_{0.9}Mn_{0.1}O_{2-\delta}$ sample.

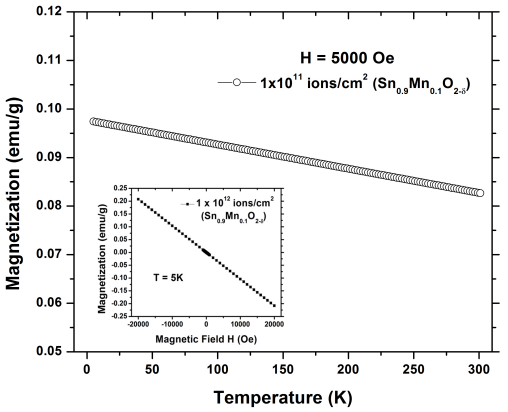

Figure 23: M vs T data measured with H = 5000 Oe for $Sn_{0.9}Mn_{0.1}O_{2-\delta}$ sample irradiated at 1×10^{11} $ions/cm^2$ fluence. The inset shows the 5K field-dependent magnetization of $Sn_{0.9}Mn_{0.1}O_{2-\delta}$ sample irradiated at 1×10^{12} $ions/cm^2$ fluence.

samples with higher carrier concentration (Pristine: $Sn_{0.9}Mn_{0.1}O_{2-\delta}$) show ferromagnetic characteristics with higher saturation magnetization and coercivity. But films irradiated at higher fluence ($\geq 1 \times 10^{12}$ $ions/cm^2$) are diamagnetic at 5 K, as shown in the inset of Fig. 23. The diamagnetic films have $n \leq 7.5 \times 10^{16}$ electrons cm^{-3}, which is much lower than that measured in ferromagnetic pristine films. We have observed that the films are ferromagnetic for the higher and intermediate range of n, 1.9×10^{20} - 3.3×10^{18} electrons cm^{-3}, and diamagnetic for lower range, $n \leq 7.5 \times 10^{16}$ electrons cm^{-3}. Thus, lowering the n from 1.9×10^{20} to 7.5×10^{16} electrons cm^{-3} results in both electrical and magnetic phase transitions, a transition from a ferromagnetic semiconducting state to a diamagnetic insulator state. For the pristine film, the M-H curve at 5 K differed by less than 6% from those measured at room temperature (300 K), from which we guess that the Curie temperature (T_C) of pristine sample is well above room temperature. But for the $Sn_{0.9}Mn_{0.1}O_{2-\delta}$ films irradiated at 1×10^{11} and 3×10^{11} $ions/cm^2$ fluence, the M-H curves at 5 K differed by 16% and 52% from those measured at room temperature, respectively. This clearly indicates that the Curie temperatures of the irradiated films are less as compared to pristine films and also decreasing on increasing the ion fluence value up to 3×10^{11} $ions/cm^2$. We also recorded the temperature (T) dependence of the magnetization (M) (field cooled) of these samples in a field of 0.5 T. Fig. 23 shows the M vs T plot for $Sn_{0.9}Mn_{0.1}O_{2-\delta}$ sample irradiated at 1×10^{11} $ions/cm^2$ fluence. The absence of any sharp drop in the M vs T data of $Sn_{0.9}Mn_{0.1}O_{2-\delta}$ sample irradiated at 1×10^{11} $ions/cm^2$ fluence suggest that the film is ferromagnetic with a Curie temperature exceeding 300 K. Magnetic measurements carried out on the pure SnO_2 films showed the expected diamagnetism with a negative magnetic susceptibility. The diamagnetic background of the pure SnO_2 film and substrate has been subtracted from all of the magnetization data shown here.

The observed room temperature ferromagnetism in pristine and irradiated $Sn_{0.9}Mn_{0.1}O_{2-\delta}$ samples cannot be due to the existence of secondary phases, because the metallic manganese and almost all of the possible manganese-based binary and ternary oxide phases (MnO, MnO_2 and Mn_2O_3) are antiferromagnetic with Neel temperature which is much less than room temperature [21]. However, $SnMn_2O_4$ and Mn_3O_4 phases are exceptions; they are ferromagnetic with Curie temperatures of 46 K and 53 K, respectively [25, 29, 194-196]. In the present work, the electron and x-ray diffraction analyses have not revealed any manganese oxide phases, although x-ray diffraction technique is not sensitive enough to detect secondary phases, if present at a very minute level. Even if these ferromagnetic secondary phases ($SnMn_2O_4$ and Mn_3O_4) are present, these cannot responsible for the ferromagnetic behavior appeared at room temperature in pristine and irradiated $Sn_{0.9}Mn_{0.1}O_{2-\delta}$ thin films. The correlation between the magnetic and electrical properties in the present $Sn_{0.9}Mn_{0.1}O_{2-\delta}$ system formulates it to be a potential aspirant for the spintronics related devices wherein the communication between the spin and charge is highly desired.

4. Conclusions

High crystalline thin films of $SnO_{2-\delta}$ and $Sn_{0.9}Mn_{0.1}O_{2-\delta}$ have been deposited by the spray pyrolysis technique and then deposited $Sn_{0.9}Mn_{0.1}O_{2-\delta}$ films have been irradiated with 120 MeV Au^{9+} ions to study the modification of structural, optical, electrical and magnetic properties. The threshold value of electronic energy loss (S_{eth}) for $Sn_{0.9}Mn_{0.1}O_{2-\delta}$ has been calculated according to Szenes' thermal spike model. The electronic energy loss (S_e) of 120 MeV Au^{9+} ions in $Sn_{0.9}Mn_{0.1}O_{2-\delta}$ is less than the threshold electronic energy loss (S_{eth}) required for the track formation in $Sn_{0.9}Mn_{0.1}O_{2-\delta}$ film. Therefore, we expect that only point defects or clusters of point defects will produce in $Sn_{0.9}Mn_{0.1}O_{2-\delta}$ thin films after irradiation. Efforts have been made to calculate equilibrium substrate/film temperature using the Stefan's equation and the calculated temperature (834 K) has been found to be quite higher than the crystallization temperature of tin oxide. This equilibrium temperature is expected to be develop within the grains of $Sn_{0.9}Mn_{0.1}O_{2-\delta}$ during irradiation period and facilitate (i) increase of grain size, (ii) removal of microstrain, and (iii) migration of point defects. The increase rate of the substrate/film temperature during irradiation has been determined by the difference between the input power density and the heat dissipation via radiation, divided by the heat capacity of the substrate. Through this it has been concluded that, in the case of high fluence, irradiation period is much longer than the amount of time needed to achieve equilibrium temperature. Therefore, in this case, the samples spend their almost full irradiation period at equilibrium temperature. This equilibrium temperature can influence the physical properties of high fluence irradiated samples. X-ray and electron diffraction patterns analysis reveals that all the unirradiated and irradiated thin films are pure crystalline with tetragonal rutile phase of tin oxide which belongs to the space group $P4_2/mnm$ (number 136). The Williamson-Hall (W-H) method has been used to evaluate the crystallite size and the microstrain of all the samples. The average crystallite size of $SnO_{2-\delta}/Sn_{0.9}Mn_{0.1}O_{2-\delta}$ nanoparticles estimated from W-H analysis and TEM/SEM/AFM analysis is highly inter-correlated. The results of electrical measurements suggest that H_O^+ defects in as-deposited $SnO_{2-\delta}$ and $Sn_{0.9}Mn_{0.1}O_{2-\delta}$ thin films are responsible for the conductivity. Through electrical investigation it has also been found that the main scattering mechanism reducing the intra-grain mobility of the electrons in pure $SnO_{2-\delta}$ films is the ionized impurity scattering. Ionized impurity scattering with singly ionized H_O^+ donor best describes the mobility of pure $SnO_{2-\delta}$ samples. Measurement of resistivity, mobility, and carrier density as a function of ion fluence (1×10^{11} to 3×10^{13} $ions/cm^2$) promulgates that increasing fluence results in degradation in electrical properties of $Sn_{0.9}Mn_{0.1}O_{2-\delta}$ film. Typical TEM micrographs of as-deposited $SnO_{2-\delta}$ and $Sn_{0.9}Mn_{0.1}O_{2-\delta}$ thin films show well isolated and highly crystallized spherical shaped crystallites. Electron diffraction patterns taken from several crystallites confirm the SnO_2 structure in both $SnO_{2-\delta}$ and $Sn_{0.9}Mn_{0.1}O_{2-\delta}$ samples and no evidence for secondary phases are observed. The SEM micrographs of as-deposited $SnO_{2-\delta}$ and $Sn_{0.9}Mn_{0.1}O_{2-\delta}$ samples reveal significant aggregation of the nanoparticles. Our AFM study demonstrates that the morphologies of irradiated films are linked with carrier concentration of target materials. If the target material is a conductor ($n \geq 10^{20} cm^{-3}$ for as-deposited $Sn_{0.9}Mn_{0.1}O_{2-\delta}$ film) then conduction electrons rapidly spread the energy of incident ion throughout the material and we find similar pristine/target sample like morphology with some dimensional change after irradiation. But if target material is an insulator (such as $Sn_{0.9}Mn_{0.1}O_{2-\delta}$ sample annealed at 850^oC) then projectile ions can not spread their energy throughout the target material and therefore they create melted region in the close vicinity of their paths. The structure of grains is changed (spherical to rod like) only when melting is observed and the nature/size of the new structure corresponded closely to the maximum molten region. In the present case, amorphous nanorods like structures may arise from overlapping and reconstruction of melted material. Further effort is under progress to explain role of carrier concentration in such morphological changes. The optical

band gap (E_g) of the films has been determined from the spectral dependence of the absorption coefficient α by the application of conventional extrapolation method (Tauc plot). For degenerate samples such as $SnO_{2-\delta}$, $Sn_{0.9}Mn_{0.1}O_{2-\delta}$ and 1×10^{11} $ions/cm^2$, it can be seen that the band gap is changing according to Burstein-Moss effect. For irradiated samples (SHI: 3×10^{11} to 3×10^{13} $ions/cm^2$), we can notice a significant but small shift in band gap from intrinsic band gap ($E_g = 3.97$ eV). This noticeable shift in the band gap upon irradiation (SHI: 3×10^{11} to 3×10^{13} $ions/cm^2$) may be due to creation of intermediate energy levels. The $Sn_{0.9}Mn_{0.1}O_{2-\delta}$ film exhibits a systematic decrease in the transmittance with increasing irradiation (SHI: 1×10^{11} - 3×10^{13} $ions/cm^2$) fluence. For highest fluence, the transmittance of the $Sn_{0.9}Mn_{0.1}O_{2-\delta}$ film is substantially reduced to about 13%. The reduction in the optical transmittance due to irradiation may result from the incorporation of V_O^0 lattice defects having absorption in the optical region. Intrinsic room temperature ferromagnetism has been observed in all degenerate films (such as pristine and irradiated (SHI: 1×10^{11} and 3×10^{11} $ions/cm^2$) $Sn_{0.9}Mn_{0.1}O_{2-\delta}$ thin films). The variation of M_S values suggest that room temperature ferromagnetism could be enhanced by increasing carrier concentration of the films. No evidence of any impurity phases are detected in $Sn_{0.9}Mn_{0.1}O_{2-\delta}$ suggesting that the emerging ferromagnetism in this system is most likely related to the properties of host SnO_2 system.

Acknowledgements

One of the authors (Sushant Gupta) is thankful to Inter University Accelerator Centre (IUAC), New Delhi for awarding Research Fellowship through the UFUP Project scheme (Project No. UFR-49311). The authors gratefully acknowledge to V. Ganesan, A. Banerjee, N. P. Lalla, M. Gupta, M. Gangrade, UGC-DAE Consortium for Scientific Research, Indore and D. Kanjilal, D. K. Avasthi, A. Tripathi, K. Asokan, P. K. Kulriya, I. Sulania, IUAC, New Delhi for providing the characterization facilities. We also thank Pelletron group, IUAC, New Delhi for expert assistance in the operation of the tandem accelerator.

References

1. H. L. Hartnagel, A. L. Dewar, A. K. Jain, C. Jagadish, Semiconducting Transparent Thin Films, IOP Publishing, Bristol, 1995.
2. J. L. Vossen, Transparent conducting electrodes, in: G. Hass, M. H. Francombe, R. W. Hoffman (Eds.), Physics of Thin Films, Vol. 9, Academic Press, New York, 1976.
3. K. L. Chopra, S. Mayor, D. K. Pandya, Transparent conductors - a status review, Thin Solid Films 102 (1983) 1-46.
4. B. G. Lewis, D. C. Paine, Applications and processing of transparent conducting oxides, MRS Bull. 25 (2000) 22-27.
5. S. Samson, C. G. Fonstad, Defect structure and electronic donor levels in stannic oxide crystals, J. Appl. Phys. 44 (1973) 4618-4623.
6. Z. M. Jarzebski, J. P. Marton, Physical properties of SnO_2 materials I: preparation and defect structure, J. Electrochem. Soc. 123 (1976) 199C-205C.
7. T. Fukumura, H. Toyosaki, Y. Yamada, Magnetic oxide semiconductors, Semicond. Sci. Technol. 20 (2005) S103-S111.
8. T. Dietl, Origin of ferromagnetic response in diluted magnetic semiconductors and oxides, J. Phys.: Condens. Matter 19 (2007) 165204:1-15.
9. W. Prellier, A. Fouchet, B. Mercey, Oxide-diluted magnetic semiconductors: a review of the experimental status, J. Phys. Condens. Matter 15 (2003) R1583-R1601.
10. J. M. D. Coey, M. Venkatesan, C. B. Fitzgerald, Donor impurity band exchange in dilute ferromagnetic oxides, Nature Materials 4 (2005) 173-179.
11. S. J. Pearton, C. R. Abernathy, M. E. Overberg, G. T. Thaler, D. P. Norton, N. Theodoropoulou, A. F. Hebard, Y. D. Park, F. Ren, J. Kim, L. A. Boatner, Wide band gap ferromagnetic semiconductors and oxides, J. Appl. Phys. 93 (2003) 1-13.
12. S. A. Wolf, D. D. Awschalom, R. A. Buhrman, J. M. Daughton, S. von Molnár, M. L. Roukes, A.

Y. Chtchelkanova, D. M. Treger, Spintronics: a spin-based electronics vision for the future, Science 294 (2001) 1488-1495.

13. S. B. Ogale, R. J. Choudhary, J. P. Buban, S. E. Lofland, S. R. Shinde, S. N. Kale, V. N. Kulkarni, J. Higgins, C. Lanci, J. R. Simpson, N. D. Browning, S. Das Sarma, H. D. Drew, R. L. Greene, T. Venkatesan, High temperature ferromagnetism with a giant magnetic moment in transparent Co-doped $SnO_{2-\delta}$, Phys. Rev. Lett. 91 (2003) 077205:1-4.
14. H. H. Nguyen, J. Sakai, N. T. Huong, N. Poirot, A. Ruyter, Role of defects in tuning ferromagnetism in diluted magnetic oxide thin films, Phys. Rev. B 72 (2005) 045336:1-5.
15. N. H. Hong, A. Ruyter, W. Prellier, J. Sakai, N. T. Huong, Magnetism in Ni-doped SnO_2 thin films, J. Phys.: Condens. Matter 17 (2005) 6533-6538.
16. N. H. Hong, J. Sakai, Ferromagnetic V-Doped SnO_2 thin films, Physica B 358 (2005) 265-268.
17. N. H. Hong, J. Sakai, W. Prellier, A. Hassini, Transparent Cr-doped SnO_2 thin films: ferromagnetism beyond room temperature with a giant magnetic moment, J. Phys.: Condens. Matter 17 (2005) 1697-1702.
18. J. M. D. Coey, A. P. Douvalis, C. B. Fitzgerald, M. Venkatesan, Ferromagnetism in Fe-doped SnO_2 thin films, Appl. Phys. Lett. 84 (2004) 1332-1334.
19. A. Punnoose, J. Hays, A. Thurber, M. H. Engelhard, R. K. Kukkadapu, C. Wang, V. Shutthanandan, S. Thevuthasan, Development of high-temperature ferromagnetism in SnO_2 and paramagnetism in SnO by Fe doping, Phys. Rev. B 72 (2005) 054402:1-14.
20. K. Gopinadhan, S. C. Kashyap, D. K. Pandya, S. Chaudhary, High temperature ferromagnetism in Mn-doped SnO_2 nanocrystalline thin films, J. Appl. Phys. 102 (2007) 113513:1-8.
21. C. B. Fitzgerald, M. Venkatesan, A. P. Douvalis, S. Huber, J. M. D. Coey, T. Bakas, SnO_2 doped with Mn, Fe or Co: Room temperature dilute magnetic semiconductors, J. Appl. Phys. 95 (2004) 7390-7392.
22. L. B. Duan, G. H. Rao, J. Yu, Y. C. Wang, G. Y. Liu, J. K. Liang, Structural and magnetic properties of chemically synthesized $Sn_{1-x}Mn_xO_2$ nanocrystalline powders, J. Appl. Phys. 101 (2007) 063917:1-6.
23. H. Kimura, T. Fukumura, M. Kawasaki, K. Inaba, T. Hasegawa, H. Koinuma, Rutile-type oxide-diluted magnetic semiconductor: Mn-doped SnO_2, Appl. Phys. Lett. 80 (2002) 94-96.
24. C. B. Fitzgerald, M. Venkatesan, L. S. Dorneles, R. Gunning, P. Stamenov, J. M. D. Coey, P. A. Stampe, R. J. Kennedy, E. C. Moreira, U. S. Sias, Magnetism in dilute magnetic oxide thin films based on SnO_2, Phys. Rev. B 74 (2006) 115307-115317.
25. K. Gopinadhan, D. K. Pandya, S. C. Kashyap, S. Chaudhary, Cobalt-substituted SnO_2 thin films: a transparent ferromagnetic semiconductor, J. Appl. Phys. 99 (2006) 126106:1-3.
26. W. Wang, Z. Wang, Y. Hong, J. Tang, M. Yu, The structure and magnetic properties of Cr/Fe-doped SnO_2 thin films, J. Appl. Phys. 99 (2006) 08M115:1-3.
27. A. Punnoose, J. Hays, V. Gopal, V. Shutthanandan, Room-temperature ferromagnetism in chemically synthesized $Sn_{1-x}Co_xO_2$ powders, Appl. Phys. Lett. 85 (2004) 1559-1561.
28. V. G. Kravets, L. V. Poperenko, Magnetic ordering effects in the Raman spectra of $Sn_{1-x}Co_xO_2$, J. Appl. Phys. 103 (2008) 083904:1-6.
29. K. Nomura, C. A. Barrero, J. Sakuma, M. Takeda, Room-temperature ferromagnetism of sol-gel synthesized $Sn_{1-x}Fe_x^{57}O_{2-\delta}$ powders, Phys. Rev. B 75 (2007) 184411:1-13.
30. A. M. Abdel Hakeem, Structure and magnetic properties of $Sn_{1-x}Mn_xO_2$, J. Magn. Magn. Mater. 324 (2012) 95-99.
31. R. Adhikari, A. K. Das, D. Karmakar, T. V. Chandrasekhar Rao, J. Ghatak, Structure and magnetism of Fe-doped SnO_2 nanoparticles, Phys. Rev. B 78 (2008) 024404:1-9.
32. P. I. Archer, D. R. Gamelin, Controlled grain-boundary defect formation and its role in the high-T_c ferromagnetism of Ni^{2+}: SnO_2, J. Appl. Phys. 99 (2006) 08M107:1-3.

33. S. K. Misra, S. I. Andronenko, K. M. Reddy, J. Hays, A. Punnoose, Magnetic resonance studies of Co^{2+} ions in nanoparticles of SnO_2 processed at different temperatures, J. Appl. Phys. 99 (2006), 08M106:1-3.
34. X. F. Liu, R. H. Yu, Mediation of room temperature ferromagnetism in Co-doped SnO_2 nanocrystalline films by structural defects , J. Appl. Phys. 102 (2007) 083917:1-5.
35. J. Hays, A. Punnoose, R. Baldner, M. H. Engelhard, J. Peloquin, K. M. Reddy, Relationship between the structural and magnetic properties of Co-doped SnO_2 nanoparticles, Phys. Rev. B 72 (2005) 075203:1-7.
36. Hyun-Suk Kim, Lei Bi, G. F. Dionne, C. A. Ross, Han-Jong Paik, Structure, magnetic and optical properties, and Hall effect of Co- and Fe-doped SnO_2 films, Phys. Rev. B 77 (2008) 214436:1-7.
37. G. A. Prinz, Magnetoelectronics, Science 282 (1998) 1660:1-3.
38. G. A. Prinz, Magnetoelectronics applications, J. Magn. Magn. Mater. 200 (1999) 57-68.
39. S. A. Chambers, R. F. C. Farrow, New possibilities for ferromagnetic semiconductors, MRS Bull. 28 (2003) 729-734.
40. N. Labedeva, P. Kuivalainen, Modeling of ferromagnetic semiconductor devices for spintronics, J. Appl. Phys. 93 (2003) 9845-9864.
41. M. D. McCluskey, M. C. Tarun, S. T. Teklemichael, Hydrogen in oxide semiconductors, J. Mater. Res. 27 (2012) 2190-2198.
42. A. K. Singh, A. Janotti, M. Scheffler, C. G. Van de Walle, Sources of electrical conductivity in SnO_2, Phys. Rev. Lett. 101 (2008) 055502:1-4.
43. P. D. C. King, T. D. Veal, Conductivity in transparent oxide semiconductors, J. Phys. Condens. Matter 23 (2011) 334214:1-17.
44. Ç. Kiliç, A. Zunger, Origins of coexistence of conductivity and transparency in SnO_2, Phys. Rev. Lett. 88 (2002) 095501:1-4.
45. Ç. Kiliç, A. Zunger, n-type doping of oxides by hydrogen, Appl. Phys. Lett. 81 (2002) 73-75.
46. W. M. Hlaing Oo, S. Tabatabaei, M. D. McCluskey, J. B. Varley, A. Janotti, C. G. Van de Walle, Hydrogen donors in SnO_2 studied by infrared spectroscopy and first-principles calculations, Phys. Rev. B 82 (2010) 193201:1-4.
47. F. Bekisli, M. Stavola, W. Beall Fowler, L. Boatner, E. Spahr, G. Lüpke, Hydrogen impurities and shallow donors in SnO_2 studied by infrared spectroscopy, Phys. Rev. B 84 (2011) 035213:1-8.
48. J. B. Varley, A. Janotti, A. K. Singh, C.G. Van de Walle, Hydrogen interactions with acceptor impurities in SnO_2: first-principles calculations, Phys. Rev. B 79 (2009) 245206.
49. P. D. C. King, R. L. Lichti, Y. G. Celebi, J. M. Gil, R. C. Vilão, H. V. Alberto, J. Piroto Duarte, D. J. Payne, R. G. Egdell, I. McKenzie, C. F. McConville, S. F. J. Cox, T. D. Veal, Shallow donor state of hydrogen in In_2O_3 and SnO_2: implications for conductivity in transparent conducting oxides, Phys. Rev. B 80 (2009) 081201:1-4.
50. K. Xiong, J. Robertson, S. J. Clark, Behavior of hydrogen in wide band gap oxides, J. Appl. Phys. 102 (2007) 083710:1-13.
51. N. Itoh, D. M. Duffy, S. Khakshouri, A. M. Stoneham, Making tracks: electronic excitation roles in forming swift heavy ion tracks, J. Phys.: Condens. Matter 21 (2009) 474205:1-14.
52. N. Itoh, A. M. Stoneham, Materials Modification by Electronic Excitation, Cambridge University Press, Cambridge, 2001.
53. D. K. Avasthi , G. K. Mehta, Swift Heavy Ions for Materials Engineering and Nanostructuring, Springer Series in Materials Science, Vol. 145, 2011.
54. M. Toulemonde, W. Assmann, C. Dufour, A. Meftah, F. Studer, C. Trautmann, Ion beam science: solved and unsolved problems, edited by P. Sigmund , Invited lectures presented at a symposium arranged by the Royal Danish Academy of Sciences and Letters, Copenhagen, 2006, pp. 263-291.
55. D. K. Avasthi, Some interesting aspects of swift heavy ions in materials science, Current Science 78 (2000) 1297-1306.

56. D. Kanjilal, Swift heavy ion-induced modification and track formation in materials, Current Science 80 (2001) 1560-1566.
57. D. K. Avasthi, J. C. Pivin, Ion beam for synthesis and modification of nanostructures, Current Science 98 (2010) 780-792.
58. R. L. Fleischer, P. B. Price, R. M. Walker, Nuclear tracks in solids: principles and applications, University of California Press, Berkeley, 1975.
59. G. Szenes, Z. E. Horvath, B. Pecz, F. Paszti, L. Toth, Tracks induced by swift heavy ions in semiconductors, Phys. Rev. B 65 (2002) 045206:1-11.
60. G. Szenes, A possible mechanism of formation of radiation defects in amorphous metals, Mater. Sci. Forum 97-99 (1992) 647-652.
61. G. Szenes, General features of latent track formation in magnetic insulators irradiated with swift heavy ions, Phys. Rev. B 51 (1995) 8026-8029.
62. G. Szenes, K. Havancsák, V. Skuratov, P. Hanák, L. Zsoldos, T. Ungár, Application of the thermal spike model to latent tracks induced in polymers, Nucl. Instr. Meth. Phys. Res. B 166-167 (2000) 933-937.
63. A. Audouard, E. Balanzat, S. Bouffard, J. C. Jousset, A. Chamberod, A. Dunlop, D. Lesueur, G. Fuchs, R. Spohr, J. Vetter, L. Thomé, Evidence for amorphization of a metallic alloy by ion electronic energy loss, Phys. Rev. Lett. 65 (1990) 875-878.
64. A. Barbu, A. Dunlop, D. Lesueur, R. S. Averback, Latent tracks do exist in metallic materials, Euro. Phys. Lett. 15 (1991) 37-42.
65. J. Henry, A. Barbu, B. Leridon, D. Lesueur, A. Dunlop, Electron microscopy observations of titanium irradiated with GeV heavy ions, Nucl. Instr. Meth. Phys. Res. B 67 (1992) 390-395.
66. B. Canut, N. Bonardi, S. M. M. Ramos, S. Della-Negra, Latent tracks formation in silicon single crystals irradiated with fullerene in the electronic regime, Nucl. Instr. Meth. Phys. Res. B 146 (1998) 296-301.
67. A. Dunlop, G. Jaskierowicz, S. Della-Negra, Latent track formation in silicon irradiated by 30 MeV fullerenes, Nucl. Instr. Meth. Phys. Res. B 146 (1998) 302-308.
68. A. Dunlop, H. Dammak, D. Lesueur, Track formation in metals by electronic processes using atomic and cluster ions, Nucl. Instr. Meth. Phys. Res. B 112 (1996) 23-25.
69. M. C. Ridgway, T. Bierschenk, R. Giulian, B. Afra, M. D. Rodriguez, L. L. Araujo, A. P. Byrne, N. Kirby, O. H. Pakarinen, F. Djurabekova, K. Nordlund, M. Schleberger, O. Osmani, N. Medvedev, B. Rethfeld, P. Kluth, Tracks and voids in amorphous Ge induced by swift heavy-ion irradiation, Phys. Rev. Lett. 110 (2013) 245502:1-5.
70. J. F. Ziegler, M. D. Ziegler, J. P. Biersack, Stopping and Ranges of Ions in Matter, SRIM Code 2008 (www.srim.org).
71. J. F. Ziegler, J. P. Biersack, U. Littmark, The Stopping and Range of Ions in Solids, Pergamon, Vol. 1, New York, 1985.
72. G. Dearnaley, Ion bombardment and implantation, Rep. Prog. Phys. 32 (1969) 405-491.
73. G. Szenes, F. Pászti, À. Péter, A. I. Popov, Tracks induced in TeO_2 by heavy ions at low velocities, Nucl. Instr. Meth. Phys. Res. B 166/167 (2000) 949-953.
74. M. Batzill, U. Diebold, The surface and materials science of tin oxide, Prog. Surf. Sci. 79 (2005) 47-154.
75. A. Berthelot, S. Hémon, F. Gourbilleau, C. Dufour, B. Domengès, E. Paumier, Behaviour of a nanometric SnO_2 powder under swift heavy-ion irradiation: from sputtering to splitting, Philosophical Magazine A 80 (2000) 2257-2281.
76. J. Nakata, Mechanism of low-temperature ($\leq 300^oC$) crystallization and amorphization for the amorphous Si layer on the crystalline Si substrate by high-energy heavy-ion beam irradiation, Phys. Rev. B 43 (1991) 14643-14668.
77. P. D. Parry, Target heating during ion implantation, J. Vac. Sci. Technol. 13 (1976) 622-629.
78. M. Kumar, P. G. Ganesan, V. N. Singh, B. R. Mehta, J. P. Singh, Nanoparticle formation by swift heavy ion irradiation of indium oxide thin film, Nanotechnology 19 (2008) 175606:1-6.

79. A. Sharma, M. Varshney, K. D. Verma, Y. Kumar, R. Kumar, Structural and surface microstructure evolutions in SnO thin films under ion irradiation, Nucl. Instr. Meth. Phys. Res. B 308 (2013) 15-20.
80. T. Mohanty, Y. Batra, A. Tripathi, D. Kanjilal, Nanocrystalline SnO_2 formation using energetic ion beam, J. Nanosci. Nanotechnol. 7 (2007) 2036-2040.
81. Wolfram language software, Wolfram Alpha LLC Company, 2014.
82. A. Janotti, J. B. Varley, J. L. Lyons, C. G. Van de Walle, Controlling the conductivity in oxide semiconductors, In: J. Wu et. al. (eds.), Functional Metal Oxide Nanostructures, Springer Series in Materials Science, 2012.
83. S. Lany, A. Zunger, Dopability, intrinsic conductivity, and nonstoichiometry of transparent conducting oxides, Phys. Rev. Lett. 98 (2007) 045501:1-4.
84. C. H. Patterson, Role of defects in ferromagnetism in $Zn_{1-x}Co_xO$: A hybrid density-functional study, Phys. Rev. B 74 (2006) 144432:1-13.
85. S. B. Zhang, S. H Wei, A. Zunger, Intrinsic n-type versus p-type doping asymmetry and the defect physics of ZnO, Phys. Rev. B 63 (2001) 075205:1-7.
86. A. F. Kohan, G. Ceder, D. Morgan, C. G. Van de Walle, First-principles study of native point defects in ZnO, Phys. Rev. B 61 (2000) 15019-15027.
87. F. Oba, S. R. Nishitani, S. Isotani, H. Adachi, I. Tanaka, Energetics of native defects in ZnO, J. Appl. Phys. 90 (2001) 824-828.
88. E. C. Lee, Y. S. Kim, Y. G. Jin, K. J. Chang, Compensation mechanism for N acceptors in ZnO, Phys. Rev. B 64 (2001) 085120:1-5.
89. P. Erhart, A. Klein, K. Albe, First-principles study of the structure and stability of oxygen defects in zinc oxide, Phys. Rev. B 72 (2005) 085213:1-7.
90. C. G. Van de Walle, Defect analysis and engineering in ZnO, Physica B 308-310 (2001) 899-903.
91. P. Erhart, K. Albe, First-principles study of migration mechanisms and diffusion of oxygen in zinc oxide, Phys. Rev. B 73 (2006) 115207:1-9.
92. A. Janotti, C. G. Van de Walle, Native point defects in ZnO, Phys. Rev. B 76 (2007) 165202-165224.
93. A. Janotti, C. G Van de Walle, Fundamentals of zinc oxide as a semiconductor, Rep. Prog. Phys. 72 (2009) 126501:1-29.
94. R. G. Parr, W. Yang, Density-Functional Theory of Atoms and Molecules, Oxford University Press, New York, 1989.
95. A. D. Becke, Density-functional thermochemistry. III. the role of exact exchange, J. Chem. Phys. 98 (1993) 5648-5652.
96. F. Trani, M. Causà, D. Ninno, G. Cantele, V. Barone, Density functional study of oxygen vacancies at the SnO_2 surface and subsurface sites, Phys. Rev. B 77 (2008) 245410:1-7.
97. A. Janotti, C. G. Van de Walle, Oxygen vacancies in ZnO, Appl. Phys. Lett. 87 (2005) 122102:1-3.
98. A. Janotti, C. G. Van de Walle, New insights into the role of native point defects in ZnO, J. Cryst. Growth 287 (2006) 58-65.
99. S. Lany, A. Zunger, Anion vacancies as a source of persistent photoconductivity in II-VI and chalcopyrite semiconductors, Phys. Rev. B 72 (2005) 035215:1-13.
100. T. R. Paudel, W. R. L. Lambrecht, First-principles calculation of the O vacancy in ZnO: a self-consistent gap-corrected approach, Phys. Rev. B 77 (2008) 205202:1-9.
101. F. Oba, A. Togo, I. Tanaka, J. Paier, G. Kresse, Defect energetics in ZnO: a hybrid Hartree-Fock density functional study, Phys. Rev. B 77 (2008) 245202:1-6.
102. J. A. Pople, P. M. W. Gill, B. G. Johnson, Kohn-Sham density-functional theory within a finite basis set, Chem. Phys. Lett. 199 (1992) 557-560.
103. J. Heyd, G. E. Scuseria, M. Ernzerhof, Hybrid functionals based on a screened Coulomb potential, J. Chem. Phys. 118 (2003) 8207.

104. L. Hedin, New method for calculating the one-particle Green's function with application to the electron-gas problem, Phys. Rev. 139 (1965) A796-A823.
105. R. W. Godby, M. Schlüter, L. J. Sham, Accurate exchange-correlation potential for silicon and its discontinuity on addition of an electron, Phys. Rev. Lett. 56 (1986) 2415-2418.
106. C. G. Van de Walle, Hydrogen as a cause of doping in zinc oxide, Phys. Rev. Lett. 85 (2000) 1012-1015.
107. G. A. Shi, M. Saboktakin, M. Stavola, S. J. Pearton, Hidden hydrogen in as-grown ZnO, Appl. Phys. Lett. 85 (2004) 5601-5603.
108. A. Janotti, C. G. Van de Walle, Hydrogen multicentre bonds, Nature Materials 6 (2007) 44-47.
109. C. G. Van de Walle, J. Neugebauer, Universal alignment of hydrogen levels in semiconductors, insulators and solutions, Nature 423 (2003) 626-628.
110. E. V. Lavrov, F. Herklotz, J. Weber, Identification of hydrogen molecules in ZnO, Phys. Rev. Lett. 102 (2009) 185502:1-4.
111. D. G. Thomas, J. J. Lander, Hydrogen as a donor in zinc oxide, J. Chem. Phys. 25 (1956) 1136-1142.
112. M. G. Wardle, J. P. Goss, P. R. Briddon, First-principles study of the diffusion of hydrogen in ZnO, Phys. Rev. Lett. 96 (2006) 205504:1-4.
113. G. A. Shi, M. Stavola, S. J. Pearton, M. Thieme, E. V. Lavrov, J. Weber, Hydrogen local modes and shallow donors in ZnO, Phys. Rev. B 72 (2005) 195211:1-8.
114. S. J. Jokela, M. D. McCluskey, Structure and stability of OH donors in ZnO from high-pressure and infrared spectroscopy, Phys. Rev. B 72 (2005) 113201:1-4.
115. C. G. Van de Walle, Hydrogen as a shallow center in semiconductors and oxides, Phys. Status Solidi B 235 (2003) 89-95.
116. E. V. Lavrov, F. Herklotz, J. Weber, Identification of two hydrogen donors in ZnO, Phys. Rev. B 79 (2009) 165210:1-13.
117. W. M. Hlaing Oo, S. Tabatabaei, M. D, McCluskey, J. B. Varley, A. Janotti, C. G. Van de Walle, Hydrogen donors in SnO_2 studied by infrared spectroscopy and first-principles calculations, Phys. Rev. B 82 (2010) 193201:1-4.
118. S. F. J. Cox, E. A. Davis, S. P. Cottrell, P. J. C. King, J. S. Lord, J. M. Gil, H. V. Alberto, R. C. Vilão, J. Piroto Duarte, N. Ayres de Campos, A. Weidinger, R. L. Lichti, S. J. C. Irvine, Experimental confirmation of the predicted shallow donor hydrogen state in zinc oxide, Phys. Rev. Lett. 86 (2001) 2601-2604.
119. E. V. Lavrov, F. Börrnert, J. Weber, C. G. Van de Walle, R. Helbig, Hydrogen-related defects in ZnO studied by infrared absorption spectroscopy, Phys. Rev. B. 66 (2002) 165205:1-7.
120. E. Mollwo, Acceptor-like deep level defects in ion-implanted ZnO, Z. Phys. 138 (1954) 478-488.
121. N. H. Nickel, Hydrogen migration in single crystal and polycrystalline zinc oxide, Phys. Rev. B 73 (2006) 195204:1-9.
122. J. Bang, K. J. Chang, Diffusion and thermal stability of hydrogen in ZnO, Appl. Phys. Lett. 92 (2008) 132109:1-3.
123. K. G. Godinho, A. Walsh, G. W. Watson, Energetic and electronic structure analysis of intrinsic defects in SnO_2, J. Phys. Chem. C 113 (2009) 439-448.
124. F. E. Akkad, S. Joseph, Physicochemical characterization of point defects in fluorine doped tin oxide films, J. Appl. Phys. 112 (2012) 023501:1-10.
125. P. D. Nola, F. Morazzoni, R. Scotti, D. Narducci, Paramagnetic point defects in SnO_2 and their reactivity with the surrounding gases. Part 1 Interaction of oxygen lattice centres with vapour-phase H_2O, air, inert and combustible gases, as revealed by electron paramagnetic resonance spectroscopy, J. Chem. Soc., Faraday Trans. 89 (1993) 3711-3713.
126. Y. Mizokawa, S. Nakamura, ESR and Electric conductance studies of the fine-powdered SnO_2, Jpn. J. Appl. Phys. 14 (1975) 779-788.
127. D. B. Granato, J. A. Caraveo-Frescas, H. N. Alshareef, U. Schwingenschlögl, Enhancement of p-type mobility in tin monoxide by native defects, Appl. Phys. Lett. 102 (2013) 212105.

128. M. D. McCluskey, S. J. Jokela, Defects in ZnO, J. Appl. Phys. 106 (2009) 071101:1-13.
129. C. G. Fonstad, R. H. Rediker, Electrical properties of high quality stannic oxide crystals, J. Appl. Phys. 42 (1971) 2911-2918.
130. M. Nagasawa, S. Shionoya, Properties of oxidized SnO_2 single crystals, Jpn. J. Appl. Phys. 10 (1971) 727-731.
131. P. Erhart, K. Albe, A. Klein, First-principles study of intrinsic point defects in ZnO: Role of band structure, volume relaxation, and finite-size effects, Phys. Rev. B 73 (2006) 205203:1-9.
132. T. R. Paudel, W. R. L. Lambrecht, First-principles calculation of the O vacancy in ZnO: a self-consistent gap-corrected approach, Phys. Rev. B 77 (2008) 205202:1-9.
133. L. S. Vlasenko, G. D. Watkins, Optical detection of electron paramagnetic resonance for intrinsic defects produced in ZnO by 2.5-MeV electron irradiation in situ at 4.2 K, Phys. Rev. B 72 (2005) 035203:1-12.
134. D. C. Look, G. C. Farlow, P. Reunchan, S. Limpijumnong, S. B. Zhang, K. Nordlund, Evidence for native-defect donors in n-type ZnO, Phys. Rev. Lett. 95 (2005) 225502:1-4.
135. D. C. Look, J. W. Hemsky, J. R. Sizelove, Residual native shallow donor in ZnO, Phys. Rev. Lett. 82 (1999) 2552-2555.
136. M. D. McCluskey, S. J. Jokela, Sources of n-type conductivity in ZnO, Phys. B: Condensed Matter 401-402 (2007) 355-357.
137. S. M. Evans, N. C. Giles, L. E. Halliburton, L. A. Kappers, Further characterization of oxygen vacancies and zinc vacancies in electron-irradiated ZnO, J. Appl. Phys. 103 (2008) 043710-043716.
138. T. Koida, H. Fujiwara, M. Kondo, Hydrogen-doped In_2O_3 as high mobility transparent conductive oxide, Jpn. J. Appl. Phys. 46 (2007) L685-L687.
139. S. Limpijumnong, P. Reunchan, A. Janotti, C. G. Van de Walle, Hydrogen doping in indium oxide: an ab initio study, Phys. Rev. B 80 (2009) 193202:1-4.
140. F. Tuomisto, K. Saarinen, D. C. Look, G. C. Farlow, Introduction and recovery of point defects in electron-irradiated ZnO, Phys. Rev. B 72 (2005) 085206:1-11.
141. Y. V. Gorelkinskii, G. D. Watkins, Defects produced in ZnO by 2.5-MeV electron irradiation at 4.2 K: Study by optical detection of electron paramagnetic resonance, Phys. Rev. B 69 (2004) 115212.
142. C. Coskun, D. C. Look, G. C. Farlow, J. R. Sizelove, Radiation hardness of ZnO at low temperatures, Semicond. Sci. Technol. 19 (2004) 752-754.
143. K. Lorenz, E. Alves, E. Wendler, O. Bilani, W. Wesch, M. Hayes, Damage formation and annealing at low temperatures in ion implanted ZnO, Appl. Phys. Lett. 87 (2005) 191904:1-3.
144. L. S. Vlasenko, G. D. Watkins, Optical detection of electron paramagnetic resonance in room-temperature electron-irradiated ZnO, Phys. Rev. B 71 (2005) 125210:1-6.
145. V. A. Nikitenko, K. $\acute{E}$. Tarkpea, I. V. Pykanov, S. G. Stoyukhin, EPR and thermoluminescence in ZnO single crystals with ionic vacancies, J. Appl. Spectrosc. 68 (2001) 502-507.
146. D. C. Look, D. C. Reynolds, J. W. Hemsky, R. L. Jones, J. R. Sizelove, Production and annealing of electron irradiation damage in ZnO, Appl. Phys. Lett. 75 (1999) 811-813.
147. D. R. Lide, CRC Handbook of Chemistry and Physics, eighty seventh edn., Taylor and Francis, London, 2005-2006, p. 12.
148. L. E. Depero, P. Levrangi, G. Sberveglieri, Structural models for cobalt-tin oxide thin films, J. Solid State Chem. 116 (1995) 256-264.
149. K. H. Kim, J. S. Chun, X-ray studies of SnO_2 prepared by chemical vapour deposition, Thin Solid Films 141 (1986) 287-295.
150. C. S. Barrett, T. B. Massalski, Structure of Metals: Crystallographic Methods, Principles and Data, third ed., McGraw-Hill, New York, 1966, p. 205.
151. H. R. Moutinho, M. M. Al-Jassim, D. H. Levi, P. C. Dippo, L.L. Kazmerski, Effects of $CdCl_2$ treatment on the recrystallization and electro-optical properties of CdTe thin films, J. Vac. Sci. Technnol, 16 (1998) 1251-1257.

152. A. Khorsand Zak, W. H. Abd. Majid, M. E. Abrishami, R. Yousefi, X-ray analysis of ZnO nanoparticles by williamson-hall and size-strain plot methods, Solid State Sci. 13 (2011) 251-256.
153. B. D. Cullity, Elements of X-ray Diffraction, Addison-Wesley Publishing Company Inc., California, 1956.
154. N. S. Ramgir, Y. K. Hwang, I. S. Mulla, J. S. Chang, Effect of particle size and strain in nanocrystalline SnO_2 according to doping concentration of ruthenium, Solid State Sci. 8 (2006) 359-362.
155. V. K. Pecharsky, P. Y. Zavalij, Fundamentals of powder diffraction and structural characterization of materials, Springer, New York, 2003.
156. G. K. Williamson, W. H. Hall, X-ray line broadening from filed Al and W, Acta Metall. 1 (1953) 22-31.
157. C. Suranarayana, M. G. Norton, X-ray Diffraction: A Practical Approach, New York, 1998.
158. E. J. Mittemeijer, U. Welzel, The "state of the art" of the diffraction analysis of crystallite size and lattice strain, Z. Kristallogr. 223 (2008) 552-560.
159. M. Lannoo, J. Bourgoin, Point Defects in Semiconductors I: Theoretical Aspects, Springer, Berlin, 1981.
160. M. Lannoo, J. Bourgoin, Point Defects in Semiconductors II: Experimental Aspects, Springer, Berlin, 1983.
161. S. T. Pantelides, Deep centers in semiconductors: A state-of-the-art approach, second ed., Gordon and Breach Science Publishers, Yverdon, 1992.
162. S. Samson, C. G. Fonstad, Defect structure and electronic donor levels in stannic oxide crystals, J. Appl. Phys. 44 (1973) 4618-4621.
163. M. Nagasawa, S. Shionoya, Properties of oxidized SnO_2 single crystals, Jpn. J. Appl. Phys. 10 (1971) 727-731.
164. S. J. Jokela, M. D. McCluskey, Structure and stability of OH donors in ZnO from high-pressure and infrared spectroscopy, Phys. Rev. B 72 (2005) 113201:1-4.
165. G. A. Shi, M. Stavola, S. J. Pearton, M. Thieme, E. V. Lavrov, J. Weber, Hydrogen local modes and shallow donors in ZnO, Phys. Rev. B 72 (2005) 195211:1-8.
166. J. R. Bellingham, W. A. Phillips, C. J. Adkins, Electrical and optical properties of amorphous indium oxide, J. Phys.: Condens. Matter 2 (1990) 6207-6221.
167. Sushant Gupta, B. C. Yadav, P. K. Dwivedi, B. Das, Microstructural, optical and electrical investigations of Sb-SnO_2 thin films deposited by spray pyrolysis, Materials Research Bulletin 48 (2013) 3315-3322.
168. R. B. Hadj Tahar, T. Ban, Y. Ohya, Y. Takahashi, Tin doped indium oxide thin films: electrical properties, J. Appl. Phys. 83 (1998) 2631-2645.
169. Sushant Gupta, The Synthesis and Characterization of Transparent Conducting Antimony Doped Tin Oxide Thin Films Deposited by Spray Pyrolysis, M.Sc. Thesis, Department of Applied Physics, Babasaheb Bhimrao Ambedkar Central University, Lucknow, India, 2012, pp. 818.
170. T. Nutz, M. Haase, Wet-chemical synthesis of doped nanomaterials: optical properties of oxygen-deficient and antimony-doped colloidal SnO_2, J. Phys. Chem. B 104 (2000) 8430-8437.
171. J. W. Orton, M. J. Powell, The Hall effect in polycrystalline and powdered semiconductors, Rep. Prog. Phys., 43 (1980) 1263-1307.
172. V. I. Fistul, V. M. Vainshtein, Mechanism of electron scattering in ln_2O_3 films, Sov. Phys. Solid State 8 (1967) 2769.
173. J. G. Na, Y. R. Cho, Y. H. Kim, T. D. Lee, S. J. Park, Effects of annealing temperature on microstructure and electrical and optical properties of radio-frequency-sputtered tin-doped indium oxide films, J. Am. Ceram. Soc. 72 (1989) 698-701.
174. V. I. Fistul, Heavily Doped Semiconductors, Plenum Press, New York, 1969, p. 86.
175. H. K. Müller, Electrical and optical properties of sputtered In_2O_3 films. I. electrical properties and intrinsic absorption, Phys. Stat. Sol. 27 (1968) 723-731.

176. H. K. Müller, Electrical and optical properties of sputtered In_2O_3 films. II. optical properties in the near infrared, Phys. Stat. Sol. 27 (1968) 733-740.
177. N. G. Deshpande, A. A. Sagade, S. D. Chavhan, J. C. Vyas, F. Singh, A. K. Tripathi, D. K. Avasthi, R. Sharma, Structural damages studies in conducting indium-tin oxide (ITO) thin films induced by Au^{8+} swift heavy ions (SHI) irradiation, Vacuum 82 (2007) 39-44.
178. P. V. Radovanovic, D. R. Gamelin, High-temperature ferromagnetism in Ni^{2+}-doped ZnO aggregates prepared from colloidal diluted magnetic semiconductor quantum dots, Phys. Rev. Lett. 91 (2003) 157202:1-4.
179. N. F. Mott, Metal-insulator transitions, Taylor and Francis, London, 1974.
180. E. Burstein, Anomalous optical absorption limit in InSb, Phys. Rev. 93 (1954) 632-633.
181. T. S. Moss, The interpretation of the properties of indium antimonide, Proc. Phys. Soc. London Ser. B 67 (1954) 775-782.
182. I. Hamberg, C. G. Granqvist, K. F. Berggren, B. E. Sernelius, L. Engstrm, Band-gap widening in heavily Sn-doped In_2O_3, Phys. Rev. B 30 (1982) 3240-3249.
183. G. Sanon, R. Rup, A. Mansingh, Band-gap narrowing and band structure in degenerate tin oxide (SnO_2) films, Phys. Rev. B 44 (1991) 5672-5680.
184. J. Tauc, R. Grogorovici, A. Vancu, Optical properties and electronic structure of amorphous germanium, Phys. Stat. Solidi. 15 (1966) 627-637.
185. S. Tsunekawa, T. Fukuda, A. Kasuya, Blue shift in ultraviolet absorption spectra of monodisperse CeO_{2-x} nanoparticles, J. Appl. Phys. 87 (2000) 1318-1321.
186. Y. S. Chaudhary, S. A. Khan, R. Shrivastav, V. R. Satsangi, S. Prakash, D. K. Avasthi, S. Dass, A study on 170 MeV Au^{13+} irradiation induced modifications in structural and photoelectrochemical behavior of nanostructured CuO thin films, Nucl. Instrum. Methods B 225 (2004) 291-296.
187. D. Mohanta, N. C. Mishra, A. Choudhary, SHI-induced grain growth and grain fragmentation effects in polymer-embedded CdS quantum dot systems, Mater. Lett. 58 (2004) 3694-3699.
188. K. L. Narayanan, K. P. Vijayakumar, K. G. M. Nair, N. S. Thampi, Effect of irradiation-induced disorder on the optical absorption spectra of CdS thin films, Physica B 240 (1997) 8-12.
189. V. Gokulakrishnan, S. Parthiban, E. Elangovan, K. Jeganathan, D. Kanjilal, K. Asokan, R. Martins, E. Fortunato, K. Ramamurthi, Investigation of O^{7+} swift heavy ion irradiation on molybdenum doped indium oxide thin films, Radiation Phys. Chem. 81 (2012) 589-593.
190. M. Kojima, H. Kato, M. Gatto, Blackening of tin oxide thin films heavily doped with antimony, Phil. Mag. B 68 (1993) 215-222.
191. I. Baia, B. Fernandes, P. Numes, M. Quiteta, R. Martins, Influence of the process parameters on structural and electrical properties of r.f. magnetron sputtering ITO films, Thin Solid Films 383 (2001) 244-247.
192. N. G. Deshpande, Y. G. Gudage, A. Ghosh, J. C. Vyas, F. Singh, A. Tripathi, R. Sharma, Studies on high electronic energy deposition in transparent conducting Indium-tin-oxide thin films, J. Phys. D: Appl. Phys. 41 (2008) 035308:1-6.
193. R. Swanepoel, Determination of the thickness and optical constants of amorphous silicon, J. Phys. E: Sci. Instrum. 16 (1983) 1214-1222.
194. K. Dwight, N. Menyuk, Magnetic properties of Mn_3O_4 and the canted spin problem, Phys. Rev. 119 (1960) 1470-1479.
195. D. G. Wickham, N. Menuyk, K. Dwight, Evidence for canted magnetic moments in manganous stannate (Mn_2SnO_4), J. Phys. Chem. Solids 20 (1961) 316-318.
196. P. Z. Si, D. Li, J. W. Lee, C. J. Choi, Z. D. Zhang, D. Y. Geng, E. Brück, Unconventional exchange bias in oxide-coated manganese nanoparticles, Appl. Phys. Lett. 87 (2005) 133122:1-3.